Experimental and Theoretical Characterization of Surface Acoustic Waves in an High Frequency 1D Phononic Crystal

Ph.D. Thesis

Scuola di Dottorato in Fisica (XXII ciclo)

Università degli Studi di Firenze

Author: **Iacopo Malfanti**

Tutor: **Dott. Renato Torre**

Coordinator of the Ph.D. School: **Prof. Alessandro Cuccoli**

December 2009

(FIS03)

To Eleonora and Neri

To the memory of Nonno Tano

`malfanti@lens.unifi.it`

Contents

Introduction and Abstract

The propagation of mechanical waves in media is a wide field of research that involves many sciences: from geology to medicine, passing through meteorology and astronomy.

After many years of scientific studies *band gap materials* are already a fundamental part of our everyday life: to think about the impact that semiconductors had on humankind in the last fifty years, justifies the above statement.
The discovery of photonic band gap materials in the late 80s made the scientific community to open towards the chance to realize light control as much as it was been achieved that of electronic properties.
It was only a matter of time to make a step beyond and to realize band gap structures for mechanical waves. Mechanical waves attracted the attention due to both their richness in the intrinsic physics (let's say the major number of polarization states with respect to electric field) and to their large relapse on many branches of sciences and technology, such as solid state physics, geophysics, architectural noise control, and substantially each field where control over mechanical waves is of importance.

Much work has been realized from a theoretical point of view, not that much has been done experimentally. Up to now most of experimental literature has concentrated on low frequency regime, while contributions at high frequencies are not many. This work has realized an experimental investigation on the propagation of high frequency surface acoustic waves over a periodically structured surface. Some new insight on the character of mechanical waves propagating in such materials have been observed. For example, in this thesis we have directly observed, for the first time, really slow waves. We will show that the slowing of mechanical waves is to be attributed to the periodic structure (*Phononic Crystal*) that was investigated. All the experimental job realized during this Ph.D. thesis has been corroborated with a theoretical analysis. In fact, simulations have been realized both to confirm the experimental data, and to have a deeper insight over mechanical waves in such structures.

The present work is divided in four chapters. The first chapter contains the main elements needed to fully comprehend the subject under study. This means that the basic notions regarding propagation of mechanical waves in periodic structures will be given along with a review of the scientific literature.
In the second chapter the samples that have been investigated and the experiment that we have realized in order to characterize them will be presented.
Third chapter is about the simulations. Here the software that we have employed together with some simulated data. During the discussion the way to perform such simulations will be clarified.
Concluding chapter is about the results that we have obtained. In particular the experimental results will be compared with those obtained by the simulations. Key points of the discussion will be the characterized *band structure*, and the direct observation of extraordinary slow waves.

Chapter 1

MECHANICAL WAVES IN PERIODIC STRUCTURES

This first chapter is devoted to a general presentation of the framework of this Ph.D. thesis. It is composed of two sections where main elements at the basis of the Phononic Crystals (PC) research will be given.

The chapter is organized as follows: in the first section the historical (not necessarily chronological) overview of this research area and some modern literature related to the thesis itself will be presented. Obviously this choice put the writer in front of the problem that along this first part some still undefined physical quantities and theories will be recalled: while the physical meaning will come directly in the discussion, their mathematical definition will be explicit only in sections two and three. The choice is guided by the desire to immediately set the reader in the PC world, instead of an ab initio development of the elastic theories to finally reach the PC. In the second section some general theoretical elements will be given: definition of equation of motion governing mechanical wave propagation in inhomogeneous samples, some general arguments about surface mechanical waves, and some notes on periodic lattice.

Before moving to the first section a fundamental question has to be answered. What is a *Phononic Crystal*? we define this as an object formed by the periodic arrangement of different elastic properties. This definition is really general, but also, to the writer's opinion, the most complete and correct one. This in fact avoid any possible confusion about the number of constituent materials, which can be even one (as vacuum cannot be considered a material!).

1.1 Notions, history and modern research

Across the end of 19^{th} century and the first part of 20^{th} century particular attention has been addressed to the problem of waves propagating in periodic potentials. Wether interested in electronic wave functions or in classical electromagnetic or mechanical waves the dispersion relation for waves propagating in such periodic materials has been subject of numerous studies and has shown to posses "bizarre" (at that time) peculiarities as forbidden frequency regions (band gaps) arising from the particular dispersion relation for these periodic systems: band structure. In spite of this early studies long time passed before scientific community was attracted by this research area.

Since then almost a century elapsed before the interest over these topics take off. In fact it was only in 1987 that two milestones papers, about propagation of light in periodically structured media, by Yablonovitch [1] and John [2] made the community starts to massively approach this subject. The era of photonic crystals was come!

As we know mechanical wave propagation deals with many phenomena, among these: earthquakes, sound and heat propagation. Ultimately Phononic Crystals (only PC frome here on) can realize the dream to have direct control at a wavelength scale over various phenomena where (tough at different characteristic length scale) the underlying physics is more or less the same. Just as in case of photonic crystals, the idea of creating materials (the word *metamaterials* would be more appropriate as it defines materials whose peculiarities arise from the realizative geometry while aren't proper of the constitutive bulk material/s) with complete acoustic (or elastic, the difference is related to the fluid or solid nature of the material in analysis. From here on, however, we will use the two words as synonyms) band gaps, i.e. frequency regions in which wave propagation is blocked for any direction inside the material, sparked a new interest in periodic elastic materials. Since 1987 photonic crystals research fuelled that on PC but a dozen years had to

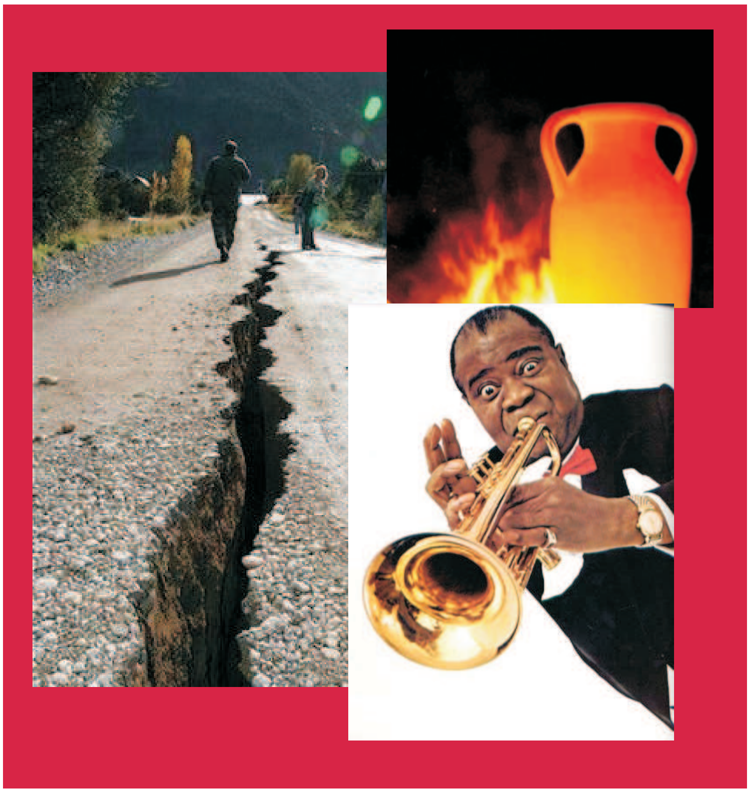

Figure 1.1: Some phenomena where mechanical waves play a fundamental role.

pass before a consistent number of publications over mechanical counterparts of photonic crystals (PC exactly) was reached in year 2000 (see Fig. 1.2). However, as early works on photonic crystals can be dated back to 1888 with the work of Lord Rayleigh [3], also PC can claim a noticeable ancestor: Leon Brillouin. His book, titled *Wave Propagation in Periodic Structures* was published at the end of Second World War in 1946, and it is curious to tell the story of the copy conserved here at University's of Florence library: it was donated from "the american people trough CARE" as a "response to Unesco reconstruction appeal". The chance for Phononic Crystals to have large impact on everyday life was even foreseen by the just established Unesco!.

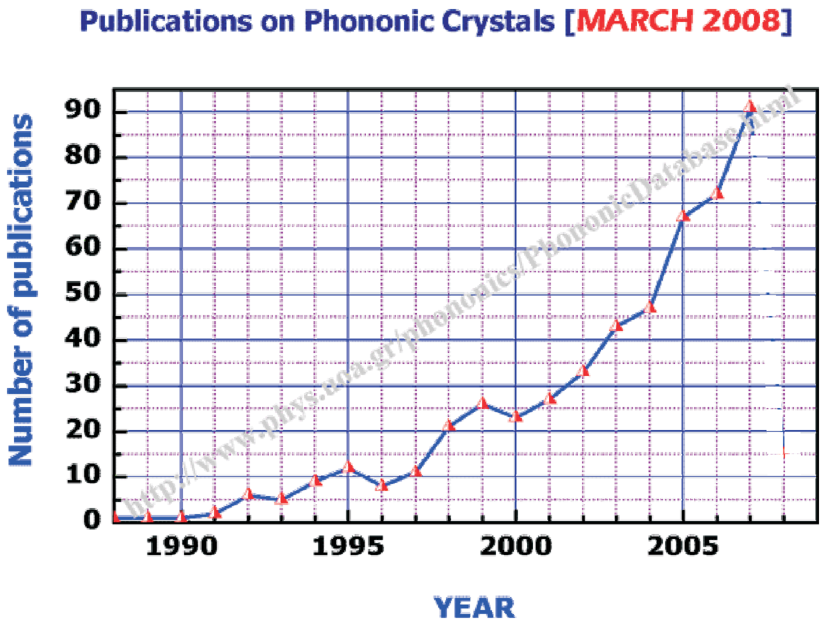

Figure 1.2: Growth of publications over Phononic Crystals, the number of publications is intended per year.

In fact potential applications are wide. They can be realized as waveguides [4] (in fact a wave, propagating in a homogeneous region sorrounded by a PC, with a characteristic frequency which falls within the band gap of the PC itself, will be guided along the path surrounded by the PC), sound barrier [5], delay lines and many other applicative objects as sound lenses [6] and the *legendary* acoustic cloak [7]. Moreover the scale invariance which applies to mechanical wave equations (as to Maxwell's equation for photonic crystals) allows to extend the operative frequency range from infrasound [8] (less than 20 Hz) to hypersonic regime [9] (GHz range). Furthermore PC notion can be applied to different mechanical wave classes as bulk waves (longitudinal or transverse character), surface waves (Rayleigh or Love type), or Lamb waves characteristic of plates [10]. Finally periodicity can be realized in one, two or three dimensional fashion.

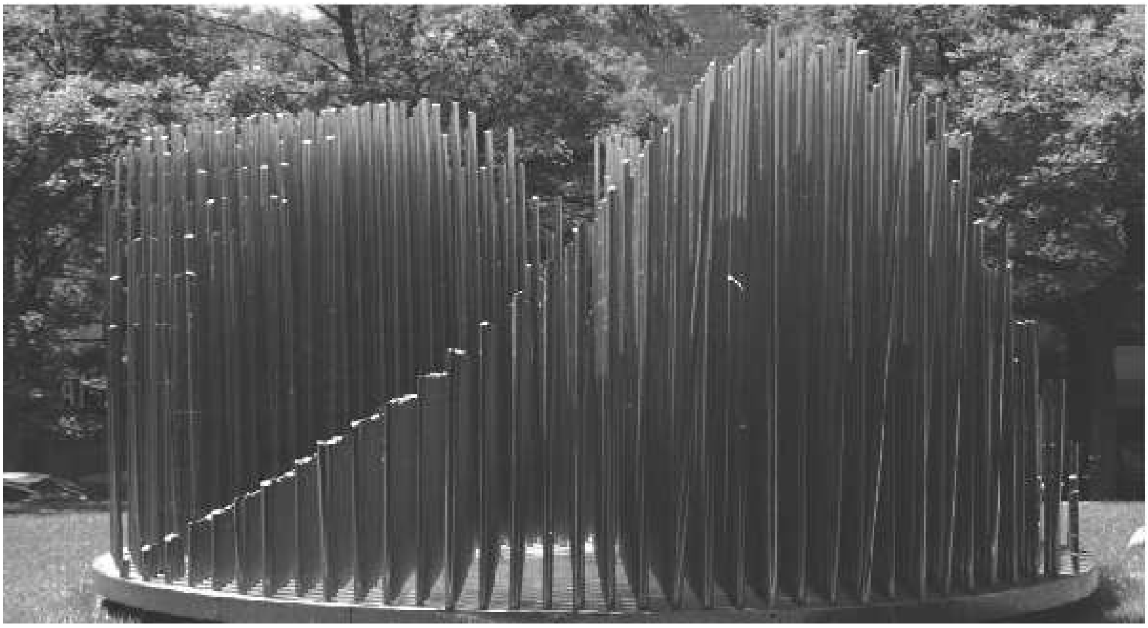

Figure 1.3: Kinetic sculpture by Eusebio Sempere, built entirely of hollow steel cylinders arranged in a periodic square array.

The search for periodic elastic composites possessing elastic band gaps was initiated by theoretical works of Kushwaha et al. with two master papers published in first half of 90s [11], [12]. Major effort in the field has initially concentrated on elucidating the conditions that favour the formation of band gaps in various type of PC (1D, 2D or 3D and solid/solid, or solid/liquid or liquid/liquid), and the dependance of band gaps width on the filling ratio (substantially, figuring the PC as a matrix with inclusion, the filling ratio is the ratio between the volume of inclusions and that of the matrix) [13], [14].

Few years later first experimental studies followed and reached notoriety after Nature's publication *Sound attenuation by sculpture* by R. Martinez-Sala et al. [15] where attenuation measurements for longitudinal waves lying in the plane orthogonal to the bars were presented, showing a band gap centered at around 1.7 KHz (see Fig. 1.3). At that time some experimental results were already present, and others followed. However, before presenting main experimental techniques trough which PC have been investigated, it is worth to stress that experimental publications over this topic are really a few when compared to theoretical ones.
Early works [16], [17] can be dated at the very birth of PC research and were realized with Brillouin Light Scatterin (BLS). These report of unexpected behaviour of the dispersion relation for Rayleigh waves (surface mode, will be back on this in the next section) in holographic gratings. The BLS technique is particulary suitable for direct band diagram characterization in fact the exchanged wave vector can be varied collecting the diffused light at different angles, allowing the band diagram reconstruction. Finally the technique is particulary appropriate for under micron PC periodicity, since smaller wave vectors would imply lower frequency Brillouin peaks that would be hardly resolved due to Rayleigh elastic peak [9], [18].
The most employed experimental technique is that which exploits mechanical transducers both to excite and reveal waves [19], [20], [21]. In this experiments sound attenuation measurements are realized. Sometimes they are referred to as tank-experiments, in that they are worked out in a filled liquid tank were the periodic solid structures embedded in the liquid realize inclusions. The technique

can be upgraded employing an imaging system in order to access the displacement field, recently negative refraction of sound was experimentally demonstrated in such an experiment [22].

Imaging not exclusively has to be related to a transducer wave source. Depending on the PC characteristic length it can be associated to optical excitation of broadband waves [23] (imaging system will obviously differ). In fact it has to be stressed that nowadays faster mechanical transducers, with the exception of interdigital transducers over piezoelectric substrates, reach up to 100 MHz which is anyhow not enough when micrometric or submicrometric structures are investigated. When considering PC with lattice step at such scale, an all optical investigation becomes necessary. As already said BLS is suitable for such structures. However two other experimental technique are available: Picosecond Ultrasonic (PU) and Transient Grating (TG) experiments. PU is a pump and probe technique [24]. The idea at the basis of this technique is to shine the sample with a short time optical laser pulse that is absorbed by the material under analysis. This causes an instantaneous thermal profile in the structure that sets up a stress field which reveals in propagative waves. The probe laser monitors the induced waves. Detection can be realized simply by monitoring the probe intensity variation due to change in the reflection coefficient (due to the induced strain) or with an interferometer that detect surface ripples [10]. Many works on PC have been realized with this technique, e.g. [10], [25], [26], [27]. PU however is not particularly suitable for band diagram characterization since the pump process generate broad band wave packet. It is on the contrary TG that shows to be the *ad hoc* technique for dispersion relation characterization. Surprisingly when this Ph.D. work was started one only paper, where PC were studied by means of the TG experiment, had been published.

Finally it should be remembered that, although the analogies with photonic crystals are many, the nature of the two types of waves (electromagnetic in the case of phononic crystals, and elastic in the case of PC) that propagates in the two classes of metamaterial is completely different. In fact, as it is well known, electromagnetic waves in isotropic media are pure transverse waves, while elastic waves can be both transverse and longitudinal. This as many implication when dealing with the solution of respective governing equations (Maxwell's equations for the electric field, mechanical equations for the *displacement field*): for PC, even in isotropic materials, the solutions of the equations directly imply the coupling between the transverse and the longitudinal displacement field so that the polarization state of the solutions is more complicated than that of the photonic crystals.

At the moment great interest is devoted to the realization of a novel class of metamaterial that results from the unification of photonic and phononic crystal properties: phoXonic crystal structures, that would allow a simultaneous control of the two types of waves [28]. As a matter of fact interaction between photons and phonons inherently takes place in a large number of optical structures and devices, and the chance to have control over these phenomena is a just developing field of research. Great deal of interest, for example, is devoted to the chance of realizing a, phonon assisted, efficient light emission in silicon. As it is known silicon present an indirect electronic bandgap so that light emission can take place only with the exchange of a phonon. The concept is then to realize a periodically arranged silicon structure to tailor phonons in order to increment the efficiency of light emission in silicon.

The challenges in front of the PC community are many and still much work has to be done.

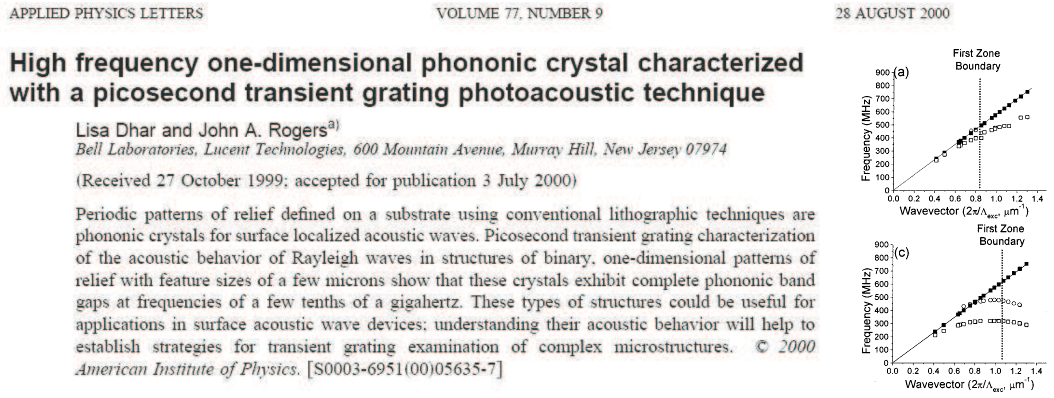

APPLIED PHYSICS LETTERS VOLUME 77, NUMBER 9 28 AUGUST 2000

High frequency one-dimensional phononic crystal characterized with a picosecond transient grating photoacoustic technique

Lisa Dhar and John A. Rogers[a)]
Bell Laboratories, Lucent Technologies, 600 Mountain Avenue, Murray Hill, New Jersey 07974

(Received 27 October 1999; accepted for publication 3 July 2000)

Periodic patterns of relief defined on a substrate using conventional lithographic techniques are phononic crystals for surface localized acoustic waves. Picosecond transient grating characterization of the acoustic behavior of Rayleigh waves in structures of binary, one-dimensional patterns of relief with feature sizes of a few microns show that these crystals exhibit complete phononic band gaps at frequencies of a few tenths of a gigahertz. These types of structures could be useful for applications in surface acoustic wave devices; understanding their acoustic behavior will help to establish strategies for transient grating examination of complex microstructures. © *2000 American Institute of Physics.* [S0003-6951(00)05635-7]

Figure 1.4: Abstract from [29]. On the right the measured relation dispersion for two samples with same realizative geometry but different characteristic parameters (e.g. lattice step).

1.1.1 Transient grating literature

Here some general aspects related to the TG existent literature over PC will be presented, other details will be given in subsections 3.3.2 and 3.3.3. The first application of TG experiment to PC characterization happened in year 2000 [29]. Since then almost a decade had to pass before another publication saw light [30]. This, probably, has to be addressed more to the complexity of a TG experiment, than to a deficiency of this experiment to give adequate information and insight over PC topic. As a matter of fact one of TG's main peculiarities is to allow dispersion relation characterization. This fully fit the PC experimental needs, since band diagram characterization give access to a complete PC knowledge. Moreover TG technique (full details will be given in next chapter) is able to cover that frequency range within 100 MHz and 1 GHz which isn't covered neither by mechanical transducers nor BLS, and, by the way, is also the operative frequency spectrum of widespread Surface Acoustic Waves (SAW) devices. These latter could highly benefit from an interplay with PC that could extend their signal analysis capability .

Both experimental works investigated the propagation of SAW on PC having a 1D periodicity but characterized by different geometrical structures. In fact reference [29] deals with periodic patterns of relief defined on a substrate (and apart for the metal film deposited on top of the corrugated surface, which doesn't alter the periodicity, is constituted by one only material, fused silica), while reference [30] investigates an elastic composite with a flat surface. In spite of these differences major results hold for the two:

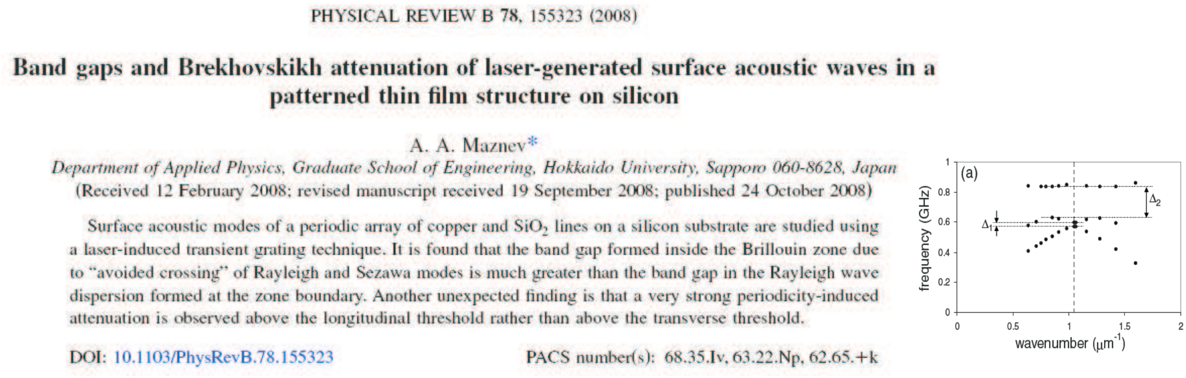

PHYSICAL REVIEW B 78, 155323 (2008)

Band gaps and Brekhovskikh attenuation of laser-generated surface acoustic waves in a patterned thin film structure on silicon

A. A. Maznev*

Department of Applied Physics, Graduate School of Engineering, Hokkaido University, Sapporo 060-8628, Japan

(Received 12 February 2008; revised manuscript received 19 September 2008; published 24 October 2008)

Surface acoustic modes of a periodic array of copper and SiO_2 lines on a silicon substrate are studied using a laser-induced transient grating technique. It is found that the band gap formed inside the Brillouin zone due to "avoided crossing" of Rayleigh and Sezawa modes is much greater than the band gap in the Rayleigh wave dispersion formed at the zone boundary. Another unexpected finding is that a very strong periodicity-induced attenuation is observed above the longitudinal threshold rather than above the transverse threshold.

DOI: 10.1103/PhysRevB.78.155323 PACS number(s): 68.35.Iv, 63.22.Np, 62.65.+k

Figure 1.5: Abstract from [30]. On the right the measured dispersion relation for one of the sample characterized.

- Both publications show phononic crystal nature of the investigated samples. This is given by the band diagram structure of the dispersion relation, and in particular by a band edge wave vector identification trough which dispersion relation is symmetric

- Presence of acoustic band gaps

- Presence of two or more modes

These arguments will be further discussed in the concluding chapter.

1.2 Theoretical elements

This section is organized in three subsections. The first one is devoted to the introduction of the dynamic equations for an inhomogeneous elastic body. The second will recall some general arguments about the propagation of surface acoustic waves. The third will recall the keynotes of periodic systems: general arguments over direct and reciprocal lattice, and the wave equation in periodic media.

1.2.1 Linear elasticity elements

Along this section mechanics of solid bodies, regarded as continuous media will be presented. References [31] and [12] are the guidelines that have been adopted here to develop the theory of elasticity, we have heavily exploited them due to their clearness.

Under the action of applied forces, solid bodies exhibit deformation, i.e. they change in shape and volume. Deformations can be defined rigorously in the following way. The position of any point in in the body is defined by its radius vector **r** (with components $x_1 = x$, $x_2 = y$, $x_3 = z$) in some coordinate system. When the body is deformed, every point in it is in general displaced. Let us consider some particular point; let its radius before deformation be **r**, and that after deformation be $\mathbf{r}'$ (with components x_i'). The displacement of this point due to the deformation is then given by the vector **r** - $\mathbf{r}'$ which we shall denote by **u**:

$$u_i = x_i' - x_i \tag{1.1}$$

The vector **u** is called the *displacement vector*. The coordinates x_i' of the displaced point depend obviously on the coordinate x_i of the point . Therefore if the vector **u** is given as a function of x_i, the deformation of the body is entirely determined. When a body is deformed, the distances between its points change. Let us consider two points very close one to another. If the radius vector joining them before deformation is dx_i, the radius vector joining the same two points when the body is deformed is $dx_i^{'} = dx_i + du_i$. The distance between the points before and after the deformation will be $dl = \sqrt{dx_1^2 + dx_2^2 + dx_3^2}$, and $dl' = \sqrt{dx_1^{'2} + dx_2^{'2} + dx_3^{'2}}$ respectively. Using the rule of summation over repeated indices we can write $dl^2 = \sum_{i=1} 3dx_i^2$, $dl'^2 = \sum_{i=1} 3dx_i^{'2} = \sum_{i=1} 3(dx_i + du_i)^2$. Substituting $du_i = (\partial u_i/\partial x_k)dx_k$ we get

$$dl^{'2} = dl^2 + 2\frac{\partial u_i}{\partial x_k}dx_i dx_k + \frac{\partial u_i}{\partial x_k}\frac{\partial u_i}{\partial x_l}dx_k dx_l \tag{1.2}$$

Since the summation is taken over both suffixes i and k in the second term, on the right hand side of the equation we can put $(\partial u_i/\partial x_k)dx_i dx_k = (\partial u_k/\partial x_i)dx_i dx_k$. In the third term, we interchange the suffixes i and l. Then $dl^{'2}$ takes the form

$$dl^{'2} = dl^2 + 2u_{ik}dx_i dx_k \tag{1.3}$$

where the tensor u_{ik} is defined as

$$u_{ik} = \frac{1}{2}(\frac{\partial u_i}{\partial x_k} + \frac{\partial u_k}{\partial x_i} + \frac{\partial u_l}{\partial x_i}\frac{\partial u_l}{\partial x_k}) \tag{1.4}$$

$$\simeq \frac{1}{2}(\frac{\partial u_i}{\partial x_k} + \frac{\partial u_k}{\partial x_i}) \tag{1.5}$$

The tensor u_{ik} is called *strain tensor* and is, by definition,symmetrical. The third term of the summation in the right hand side of eq. (1.4) can be dropped down when small deformations are considered , i.e. *linear elasticity* approximation is considered (eq. (1.5)). We will assume that this approximation applies to the investigated samples.

In a body that is not deformed, the arrangement of molecules corresponds to a state of thermal equilibrium, then all parts of the body are in mechanical equilibrium.

When a deformation occurs molecule's arrengment is changed, and the body ceases to be at rest. Therefore the body returns to the original equilbrium state by means of forces that arises due to the deformation itself. This internal forces are known as *internal stresses*, and in the following we will consider that internal stresses are only governed by elastic forces (Hooke's law) without any contribution from eventual stresses arising from pyroelectric or piezoelectric effects.

We can now write down the equations of dynamics. We consider an inhomogeneous, however isotropic and linearly elastic solid of infinite extension. At every point $\mathbf{r}$ the medium is characterized by three purely mechanical parameters: the mass density $\rho(\mathbf{r})$, the longitudinal speed of sound $c_l(\mathbf{r})$ and the transverse speed of sound $c_t(\mathbf{r})$. In terms of these the stress tensor assumes the form

$$\sigma_{ij} = 2\rho c_t^2 u_{ij} + \rho(c_l^2 - c_t^2)u_{ll}\delta_{ij} \tag{1.6}$$

where the summation over repeated indices (throughout all the text) convention is adopted, then Newton's law of dynamic reads [12]

$$\begin{aligned} \rho\frac{\partial^2 u_i}{\partial t^2} &= \frac{\partial \sigma_{ij}}{\partial x_j} \qquad (1.7)\\ &= \rho c_t^2 \nabla^2 u_i + \rho(c_l^2 - c_t^2)\frac{\partial}{\partial x_i}\nabla\cdot\mathbf{u} + \nabla(\rho c_t^2)\cdot\nabla u_i \qquad (1.8)\\ &+ \nabla(\rho c_t^2)\cdot\frac{\partial \mathbf{u}}{\partial x_i} + [\frac{\partial}{\partial x_i}(\rho c_l^2 - 2\rho c_t^2)]\nabla\cdot\mathbf{u} \qquad (1.9) \end{aligned}$$

after some algebra this can be brought into the form

$$\rho\frac{\partial^2 u_i}{\partial t^2} = \nabla\cdot(\rho c_t^2\nabla u_i) + \nabla\cdot(\rho c_t^2\frac{\partial}{\partial x_i}\mathbf{u}) + \frac{\partial}{\partial x_i}[(\rho c_l^2 - 2\rho c_t^2)\nabla\cdot\mathbf{u}] \tag{1.10}$$

Equation (1.10) represents the elastic wave equation for an inhomogeneous elastic medium. It is somehow complicated, with respect to that of an homogeneous medium, since with ρ, c_l and c_t being position dependent the equation *cannot* be separated into two independent equations, one for the longitudinal displacement (that satisfies $\nabla\times\mathbf{u} = 0$) and the other for the transverse displacement (with $\nabla\cdot\mathbf{u} = 0$).

1.2.2 Surface Acoustic Waves

Here some general notions about waves propagating at the free surface of a body will be considered. The approach to the surface waves theory presented here is not intended to be neither complete, nor detailed or analytical, but, instead, will only focus on general aspects of main interest to this Ph.D. thesis: qualitative key points on some specific types of surface waves will be presented here.

Let us consider the case of a homogeneous, isotropic finite media. Bulk waves will continue to be a solution of the equations (1.10) but other solution are present at the boundaries of the body (on the surface).

Let us consider the sagittal plane (in red in Fig. 1.6), that is the plane containing both the normal to the surface and the wave vector (lying in the surface), it can be shown that surface waves contained in this plane are decoupled from those in the plane orthogonal to the sagittal one. Surfaces acoustic waves (SAW) contained in the sagittal plane are semi-transverse (longitudinal and transverse displacements aren't decoupled). They're usually referred to as *Rayleigh waves*. SAW lying in the plane orthogonal to the sagittal plane will have a pure transverse character and are known as *Love waves*. In the rest of this thesis only Rayleigh SAW will be considered (sometime only the acronym SAW will be used).

The equation of motion predicts, in the case of an homogeneous body, a single SAW mode (the Rayleigh mode) which is non dispersive (upper right part in Fig. 1.6). The sound speed c_R have an empirical expression given by the Viktorov formula

$$c_R \simeq \frac{0.87 + 1.12\nu}{1+\nu} c_t \tag{1.11}$$

where ν is the Poisson's ratio. Obviously $c_R < c_t$.

The Rayleigh is a guided mode, the associated displacement field decays exponentially with depth in the material. At a depth of some wavelengths, no displacement is associated to the wave propagating at the surface.

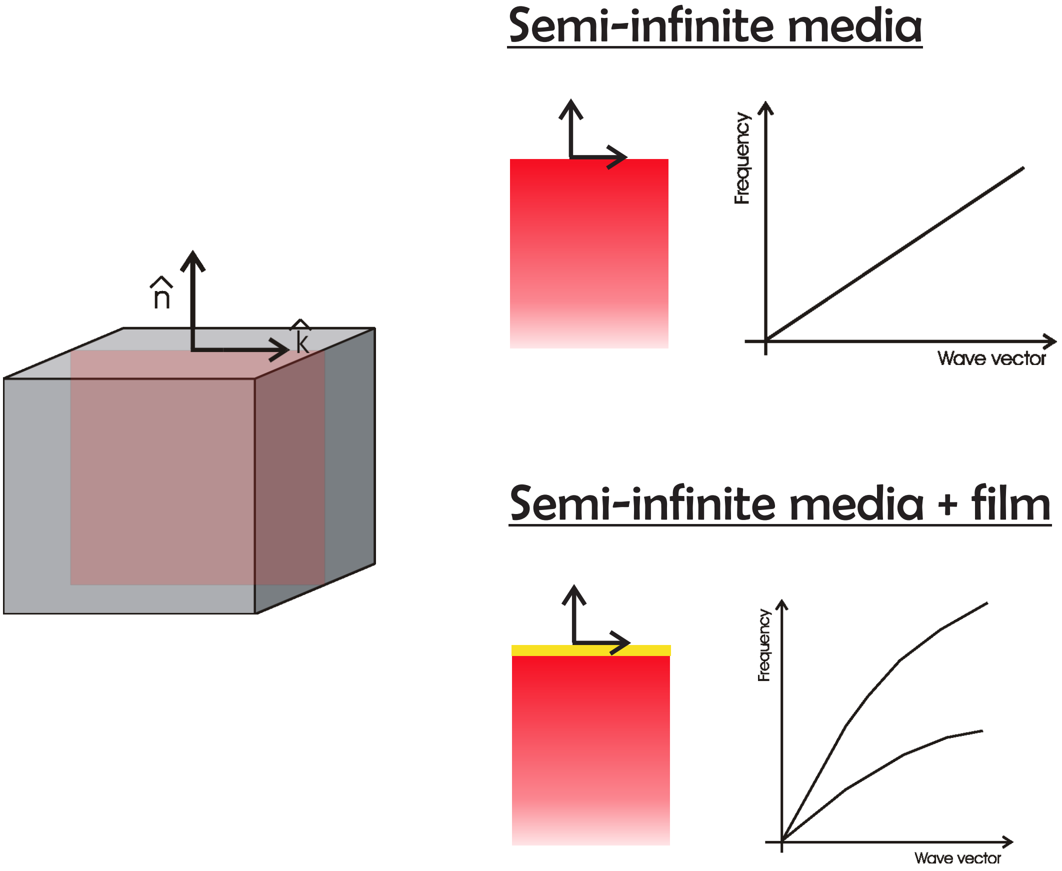

Figure 1.6: In red the sagittal plane. Two different cases are that of a free homogeneous surface of a semi-infinite media or that of a film bounded to the surface. Different dispersion relation are related to the two cases.

In order to perform our experimental investigation of SAW we are forced to use samples characterized by an high reflection coefficient. This is achieved realizing a thin metal film on the sample surface. The equation of motion of the system is then modified and hence the SAW definition [32].

When a film is bounded to the surface several modes can be guided along the surface (lower right part in Fig. 1.6). Two general cases can be distinguished: "fast" films over "slow" substrates, and viceversa. We will focus on the latter case

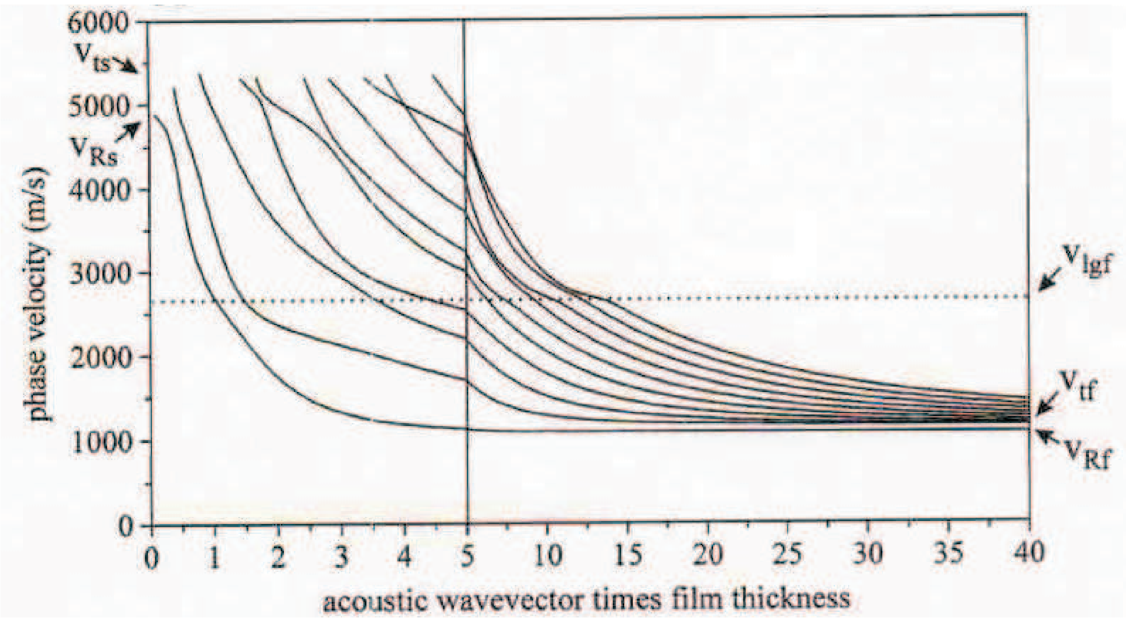

Figure 1.7: Dispersive character of the modes guided along the surface of a body constituted by a "fast" substrate and a "slow" film. In this graph the phase velocity is plotted against the product of the wavector associated to the wave and the film thickness [32]. To interprete the meaning of the indicated values please note that: V stands for velocity, the subscript t (R, lg) for transverse (Rayleigh or longitudinal respectively), while subscript s (f) is indicating a substrate (or film) property.

("slow" films over "fast" substrates) as the samples studied along this Ph.D. work fit this class. As it has been said many dispersive modes can be supported. To clarify the behaviour of these surface waves (generally first order mode is named Rayleigh mode and higher orders are called Rayleigh-Sezawa modes or simply higher order Rayleigh modes) the Fig. 1.7 taken from [32] results useful. Here the phase velocity of the wave is plotted against the product of the wave vector (k) associated to the wave itself and the film thickness (h).

As it can be seen depending on the kh value more modes can be supported by the surface. For high values of kh (a film thickness much bigger than the wavelength of the wave itself) the displacement will mainly involve the film itself and its properties will be sensed. In fact, as shown in Fig. 1.7, the Rayleigh mode will have a velocity that at limit approaches the Rayleigh velocity of the film while Rayleigh-Sezawa modes will tend to the film's transverse velocity.

For low values of the product kh (that means waves characterized by a wavelength much bigger than the film thickness) the first mode approaches the value of the Rayleigh mode of the substrate. Higher order mode have a phase velocity cutoff (we'll be back on the meaning of this cutoff in last chapter) given by the transverse velocity of the substrate itself. In some way when the wavelength is much bigger than the film thickness the wave *senses* only a little the presence of the film as the wave's associated displacement involves (penetrating in depth for about a wavelength) mainly the substrate.

In the experimental investigation reported in this work the product $kh < 0.14$ so that the substrate properties can be easily investigated.

1.2.3 Periodic systems and lattices

As this thesis deals mainly with waves propagating in spatially periodic structures, here we want to recall the basic properties and definition over such structures.

The starting point in the description of the symmetry of any periodic arrangement is the concept of *Bravais* lattice. The Bravais Lattice is defined as an infinite spatial array of discrete points with such an arrangement and orientation that it appears exactly the same from whichever of its points the array is viewed [33]. Mathematically, a three dimensional Bravais lattice is defined as a collection of point with position vectors $\mathbf{R}$ of the form

$$\mathbf{R} = \sum_{i=1}^{3} m_i \mathbf{a}_i \tag{1.12}$$

with $\mathbf{a}_i$ any three generic vectors laying in different planes and joining two points of the lattice; and m_i any integer numbers. Vectors $\mathbf{a}_i$ are called *primitive* vectors of a given Bravais lattice (the choice of these primitive vectors is not unique as shown in Fig. 1.8). When one (two) of the primitive vectors is (are) zero the equation (1.12) defines a two (one) dimensional Bravais lattice as in Fig. 1.8. Another fundamental concept of spatial lattices is that of *primitive cell.* The primitive cell is a volume of space that contains precisely one lattice point and can be translated trough all the vectors of a Bravais lattice to fill all the space without overlapping itself or leaving voids. The most common choice is however the *Wigner-Seitz cell* (WSC), which has full symmetry of the underlying Bravais lattice. It can be constructed drawing lines connecting a given point to nearby lying points, bisecting each line and taking the smallest polyhedron bounded by these planes (dark grey area in Fig. 1.8).

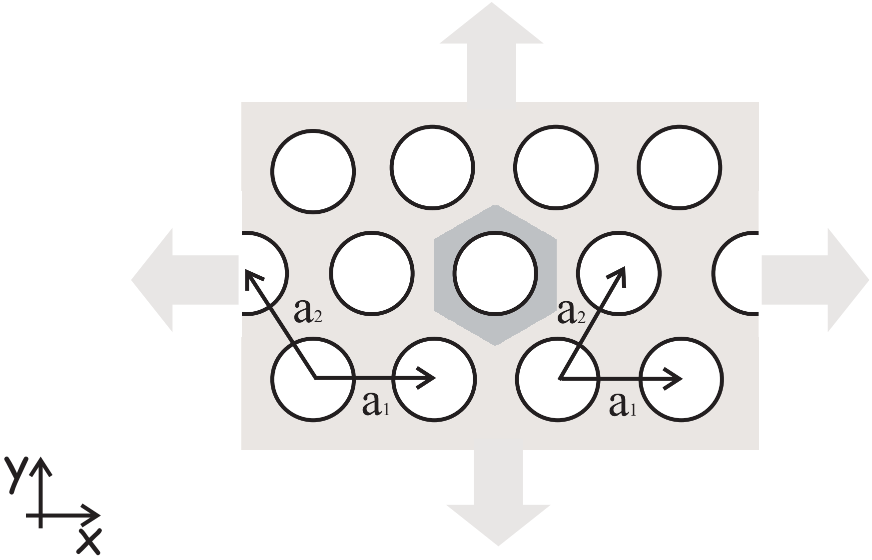

Figure 1.8: A 2D triangular Bravais lattice. Some, between many, possible choices of the primitive vectors a_1 and a_2. Dark grey area represents the Wigner-Seitz cell.

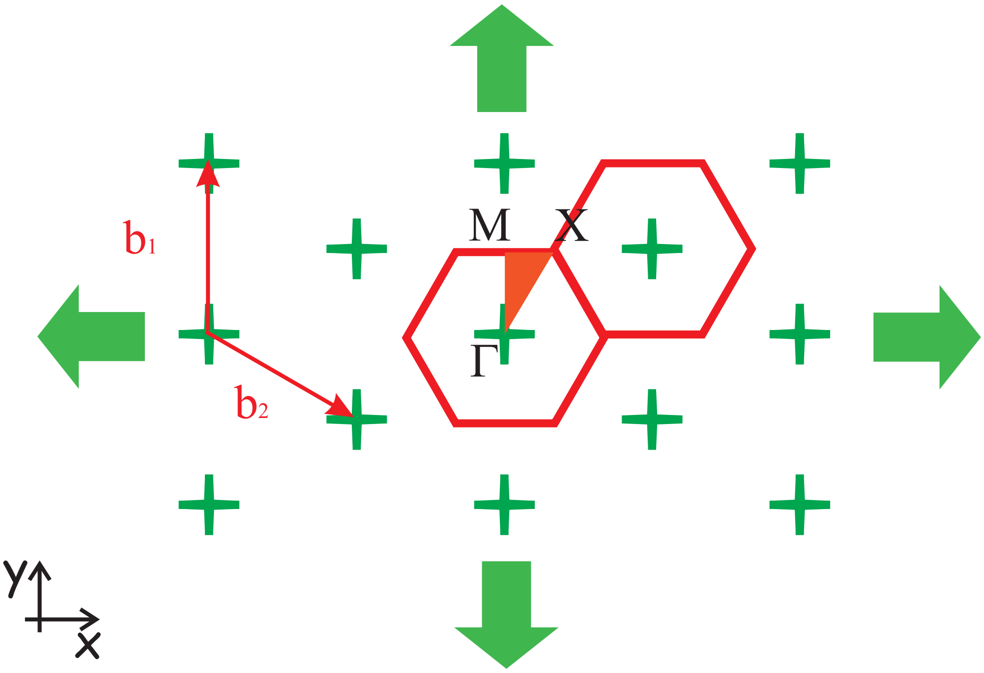

Figure 1.9: The reciprocal lattice of the 2D triangular Bravais lattice shown in Fig. 1.8 is (arbitrary) represented with green crosses. It is a triangular lattice as the direct one. The reciprocal lattice is rotated of 30° with respect to direct lattice. The same applies to the WSC. In red the basis resulting from the the direct basis choice $\mathbf{a}_1$ and $\mathbf{a}_2$ shown on the right of Fig. 1.8. Green arrows indicate that the lattice has infinite extent.

The Bravais lattice, which is defined in *real* space, is sometimes referred to as *direct* lattice. At the same time there exists the concept of *reciprocal* lattice, which play a fundamental role in virtually any study of any wave phenomena in periodic structures. For any Bravais lattice $\mathbf{R}$ in real space given by equation (1.12) there exist a set of wavectors $\mathbf{G}$, that constitute the *reciprocal* lattice in the reciprocal space (the space of wave vectors), satisfying

$$e^{[i\cdot(\mathbf{G}\cdot\mathbf{R})]} = 1 \tag{1.13}$$

for every $\mathbf{R}$ in the direct lattice. The reciprocal lattice is a Bravais lattice itself.

The primitive vectors $\mathbf{b}_i$ of the reciprocal lattice are constructed from the primitive vectors $\mathbf{a}_i$ of the direct lattice by the following expressions

$$\begin{aligned} \mathbf{b}_1 &= 2\pi \frac{\mathbf{a}_2 \wedge \mathbf{a}_3}{\mathbf{a}_1 \cdot (\mathbf{a}_2 \wedge \mathbf{a}_3)} \\ \mathbf{b}_2 &= 2\pi \frac{\mathbf{a}_3 \wedge \mathbf{a}_1}{\mathbf{a}_2 \cdot (\mathbf{a}_3 \wedge \mathbf{a}_1)} \\ \mathbf{b}_3 &= 2\pi \frac{\mathbf{a}_1 \wedge \mathbf{a}_2}{\mathbf{a}_3 \cdot (\mathbf{a}_1 \wedge \mathbf{a}_2)} \end{aligned} \tag{1.14}$$

As the reciprocal lattice is a Bravais lattice one can identify its WSC, conventionally called *first Brillouin zone* (contained within the red hexagon in Fig. 1.9). Of particular interest is the *irreducible* Brillouin zone (ZIB) (red area in Fig. 1.9) along whose boundaries the properties of the periodic medium under analysis can be fully characterized.

The equation (1.10) is valid for an arbitrary inhomogeneity. Now we focus on inhomogeneous material which exhibits spatial periodicity. This implies that all the material properties $\rho(\mathbf{r})$, $c_l(\mathbf{r})$ and $c_t(\mathbf{r})$ may be expanded in Fourier series. Actually it is convenient to expand ρc_l^2 and ρc_t^2 rather than c_l and c_t themselves [12]

$$\begin{aligned} \rho(\mathbf{r}) &= \sum_{\mathbf{G}} \rho(\mathbf{G}) e^{i\mathbf{G}\cdot\mathbf{r}} \\ \rho(\mathbf{r}) c_l^2(\mathbf{r}) &= \sum_{\mathbf{G}} \Lambda(\mathbf{G}) e^{i\mathbf{G}\cdot\mathbf{r}} \\ \rho(\mathbf{r}) c_t^2(\mathbf{r}) &= \sum_{\mathbf{G}} \tau(\mathbf{G}) e^{i\mathbf{G}\cdot\mathbf{r}} \end{aligned} \tag{1.15}$$

The periodicity of the medium may be three, two or one dimensional, the reciprocal lattice vector has corresponding dimensionality. The summation in (1.15) extends over the infinite reciprocal lattice that correspond to the Bravais lattice in real space. The displacement, associated to the generic wave vector $\mathbf{k}$, $\mathbf{u}_{\mathbf{k}}(\mathbf{r})$ must satisfy the Bloch theorem

$$\mathbf{u_k}(\mathbf{r}) = e^{i(\mathbf{k}\cdot\mathbf{r}-\omega t)} \sum_{\mathbf{G}} \hat{\mathbf{u}}_{\mathbf{k}}(\mathbf{G}) e^{i\mathbf{G}\cdot\mathbf{r}} \tag{1.16}$$

where ω is the circular frequency of the wave. Substitution of equations (1.16) and (1.15) in equation (1.10), and the use of some vector algebra together with the multiplication by $exp(-i\mathbf{G}''\cdot\mathbf{r})$ and integration over the unit cell, gives the result

$$\sum_{\mathbf{G}'}\{\tau(\mathbf{G}-\mathbf{G}')\mathbf{u_k}(\mathbf{G}')(\mathbf{k}+\mathbf{G}')\cdot(\mathbf{k}+\mathbf{G})+\tau(\mathbf{G}-\mathbf{G}')\mathbf{u_k}(\mathbf{G}')\cdot(\mathbf{k}+\mathbf{G})(\mathbf{k}+\mathbf{G}')+ \tag{1.17}$$

$$+[\Lambda(\mathbf{G}-\mathbf{G}')-2\tau(\mathbf{G}-\mathbf{G}')]\mathbf{u_k}(\mathbf{G}')\cdot(\mathbf{k}+\mathbf{G}')(\mathbf{k}+\mathbf{G})-\omega^2\rho(\mathbf{G}-\mathbf{G}')=0$$

If we allow $\mathbf{G}$ to take all the points of the reciprocal lattice, then equation (1.17) is an infinite set of linear equations for the eigenvectors $\mathbf{u_k}(\mathbf{G})$. For a given value of the wave vector $\mathbf{k}$ this set of equations has solution for some eigenvalues $\omega_n(\mathbf{k})$, where $n = 1, 2, ...$ is the first, second, etc. vibrational band. Then if we plot the eigenvalues ω_n obtained for the values of the Bloch wave vector $\mathbf{k}$ along the ZIB we obtain the so-called *band diagram*, which is nothing else than the relation dispersion characteristic of the periodic system under study.

Chapter 2

SAMPLES AND EXPERIMENTAL TECHNIQUE

This chapter is composed of two main sections. In the first one a detailed presentation of the experimental technique adopted to investigate the sample and a theoretical analysis of the measured signal will be given. In the second section the investigated samples will be presented.

2.1 Transient Grating experiment

The Transient Grating experiment (TG) is a time resolved optical technique, based on non linear optical effects [34], it is indeed a particular case of the large category of the so called four-wave-mixing techniques [35, 36]. This experimental tool is particularly suitable to measure mechanical, acoustic, viscous and thermal phenomena in solids as in liquids. It enables the investigation of a very wide temporal range, from nanosecond to millisecond. Thanks to the Heterodyne Detection (HD) (a detailed description will follow) the measured signal is characterized by an excellent signal to noise ratio. Definitely, HD-TG experiments can be considered an important breakthrough within the framework of the optical techniques, because of their capability to measure many different dynamics in a time window where alternative methods fail.

It has to be stressed that two possible configurations of the experiment are possible:

- Transmission geometry: suitable to investigate bulk properties of semi-transparent materials.
- Reflection geometry: suitable to investigate superficial properties of reflecting media.

As already pointed out during this Ph.D. work all measurement have been realized in this latter configuration.

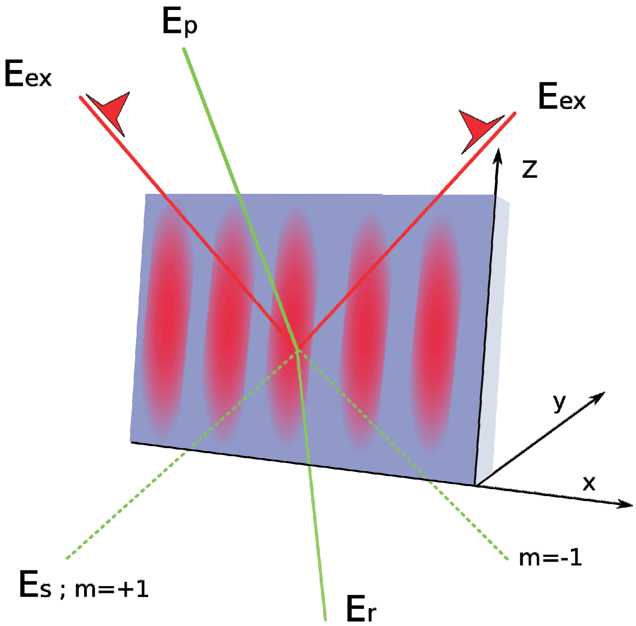

Figure 2.1: Schematic drawing of a transient grating experiment in reflection geometry. Two excitation pulses, induce an impulsive spatial modulation of the dielectric constant. The relaxation of the induced transient modulation is probed by a third beam E_p. The signal field $\mathbf{E}_s$ is the first order reflected diffracted field.

In general, in a TG experiment two laser pulses, obtained dividing a single pulsed laser beam, are made to interfere on a sample (over its surface or in bulk depending on the mechanical waves under study) and generate a spatially periodic variation of the optical material properties (e.g. refractive index) due to radiation-matter interaction phenomena. [36–38].This modulation is probed by a third laser beam, typically of different wavelength from that of the pump; it can be either a pulsed or a continuous-wave (CW) beam. It impinges on the induced grating and it is subsequently diffracted by it (be it reflected or transmitted). The diffracted signal provides information on the relaxing grating, then on the induced dynamics.

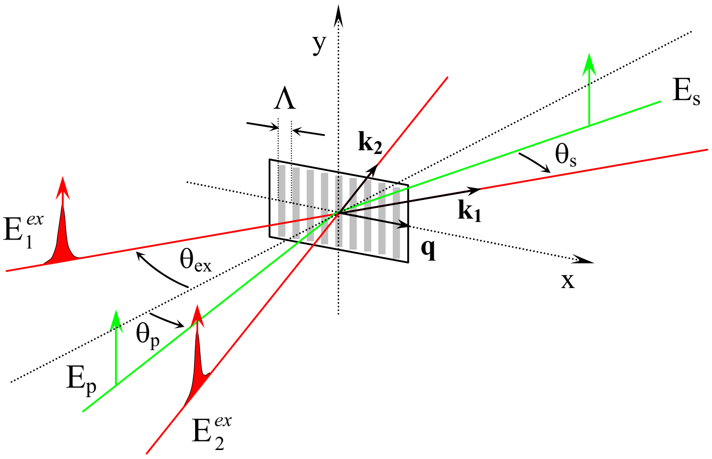

Figure 2.2: Schematic drawing of a transient grating experiment in transmission geometry. Two excitation pulses, E_1^{ex} and E_2^{ex} induce an impulsive spatial modulation of the dielectric constant with step Λ. The relaxation of the induced transient modulation is probed by a third beam, E_p.

Schematic drawings of a TG experiment are shown in Fig. 2.1 and Fig.2.2. To be as clear as possible the details are shown in the transmission geometry figure, however the same holds for the reflection geometry. The spatial modulation is characterized by the wave-vector $\mathbf{q}$, equal to the wave-vector difference $(\mathbf{k}_1 - \mathbf{k}_2)$ of the two pump pulses. Its modulus is:

$$q = \frac{4\pi \sin(\theta_{ex})}{\lambda_{ex}}, \tag{2.1}$$

where λ_{ex} and θ_{ex} are the wavelength and the incidence angle of the exciting pulses, respectively.

2.1.1 Signal definition

Concentrating over excitation of surface acoustic waves in metals we consider that radiation-matter interaction between pump light and metallic surface is dominated by absorption phenomena due to free electrons. In fact the free electrons rapidly absorb pump light and instantaneously (relatively to the experimental temporal resolution, that corresponds to few tens of picoseconds) relax via non-radiative channels generating a local heating. So that, soon after pump light absorption, the interference optical grating rapidly turns into a temperature grating. The rapid conversion of electromagnetic energy into heat enables to separate the pump process from the probing.

The probe process consists in detecting the first order reflected diffracted field $\mathbf{E}_s$ (shown in Fig. 2.1) of the probe field $\mathbf{E}_p$ (wave vector $\mathbf{k}_p$). To what the wave vector $\mathbf{k}_s$ of $\mathbf{E}_s$ is involved, normal reflection rules apply to the y and z component ($k_{s\,y} = -k_{p\,y}$, $k_{s\,z} = k_{p\,z}$), while the x component of the diffracted field is related to the diffraction from the induced grating

$$k_{s\,x} = k_{p\,x} + q. \tag{2.2}$$

In order to define the measured signal it is useful to introduce the ratio between the amplitude of the i-th component (the 1,2,3 indices stand for x,y,z axis) of the probe field $E_{p\,i}$ and that of the electromagnetic field $E'_{p\,i}$, given by the interaction of the probe beam with the metallic surface eventually modified from the gratings generated by the pump light absorption (we will illustrate these phenomena in the following), in the very surface proximity

$$E'_{p\,i}(x, y, z = \epsilon, t) = R_{ij} E_{p\,j} \tag{2.3}$$

The $E'_{p\,i}$ distribution generates, in the far field condition the reflected field and the diffracted beams. The ij element of the complex reflection tensor R is defined as the product of an amplitude and a phase term

$$R_{ij} = r_{ij} e^{i \cdot \varphi_{ij}} \tag{2.4}$$

In what way a grating induced on the surface affects this field? The pump induced grating results as a thin, sinusoidal amplitude and phase grating along the surface (which is, moreover, no longer flat but sinusoidally rippled due to thermal expansion, with a ripple amplitude ϵ around the flat value z=0. This turns to be an extra phase-grating contribution that, only for the moment, we neglect). Since modulations of the pump induced gratings are weak the two effects can be considered, in first approximation, as independent.

The amplitude modulation produce a field distribution at the very surface proximity

$$E'_{p\,i} = [r_{ij} + \Delta r_{ij}(t) \cos(qx)] e^{i \cdot \varphi_{ij}} E_{p\,j} \tag{2.5}$$

where $\Delta r_{ij}(t) \cos(qx)$ is the amplitude variation of the ij element of the reflection tensor induced by the amplitude transient grating. The reflected electromagnetic field and the diffracted orders fields in the far-field approximation (distance y from the surface satisfies $y >> \Lambda^2/\lambda$, with λ electromagnetic wavelength) can be obtained within the framework of Fourier optics and is proportional to the Fourier transform of the electromagnetic field distribution at the surface [39]. It can be shown that the *first order* reflected diffracted field (E_s) distribution is then

$$E_{s\,i} \propto \Delta r_{ij}(t, q) E_{p\,j} \tag{2.6}$$

Similarly the phase modulation generated by the grating induces a field distribution

$$E'_{p\,i} = r_{ij} e^{i\cdot[\varphi_{ij}+\Delta\varphi_{ij}(t)\cos(qx)]} E_{p\,j} \tag{2.7}$$

where $\Delta\varphi_{ij}(t)\cos(qx)$ is the phase variation in the ij element of the reflection tensor induced by the transient phase grating. In this case, it can be shown that the first order reflected diffracted field distribution is

$$E_{s\,i} \propto i\Delta\varphi_{ij}(t,q) E_{p\,j} \tag{2.8}$$

When a phase grating and an amplitude grating are present at the same time and weak grating approximation is considered (induced variations are few percentage of the unperturbed reflection coefficients), the previous results still hold for the sum of the two contributions: first order diffracted reflected field is simply proportional to the sum of the induced variations

$$E_{s\,i} \propto [\Delta r_{ij}(t,q) + i\Delta\varphi_{ij}(t,q)] E_{p\,j} \tag{2.9}$$

The reflectivity tensor is defined by the dielectric tensor ϵ_{ij} and so to the experimental observables. In a metal the dielectric tensor is complex

$$\epsilon_{ij} = \epsilon'_{ij} + i\epsilon''_{ij} \tag{2.10}$$

It can be shown that [40] transient grating induced variations Δr_{ij} and $\Delta\varphi_{ij}$ can be written in terms of transient grating induced variations of the real and imaginary components of dielectric tensor as

$$\Delta r_{ij} = a\Delta\epsilon'_{ij} + b\Delta\epsilon''_{ij} \tag{2.11}$$

$$\Delta\varphi_{ij} = c\Delta\epsilon'_{ij} + d\Delta\epsilon''_{ij} \tag{2.12}$$

where the constants a, b, c, and d are parameters proper of the metal considered. In conclusion the real and imaginary part of the dielectric variation tensor can be expressed in terms of the temperature T and the strain u_{ij} as

$$\Delta\epsilon'_{ij} = \frac{\partial\epsilon'_{ij}}{\partial T}\delta_{ij}dT + P'_{ijkl}u_{kl} \tag{2.13}$$

$$\Delta\epsilon''_{ij} = \frac{\partial\epsilon''_{ij}}{\partial T}\delta_{ij}dT + P''_{ijkl}u_{kl} \tag{2.14}$$

where P'_{ijkl} and P''_{ijkl} are respectively the real and imaginary part of the complex elasto-optic tensor. It is immediately realized then, that both the temperature grating and the elasto-optic strains grating (instantaneously induced by the temperature grating itself) contribute to realize the amplitude (phase) grating which results in $\Delta r_{i,j}(q,t)$ ($\Delta\varphi_{ij}(q,t)$).

Finally we should consider the extra-contribution to the signal given by the rippled surface. As we have said the ripples are generated by the thermal expansion so that the surface is displaced. Along the x direction the ripples realize a sinusoidal grating for the displacement. The vertical displacement profile, initially set up by thermal expansion, is given by $u_y = \epsilon(t)cos(qx)$. This is a sinusoidal phase grating associated to the surface vertical profile and its contribution to the phase variation in the ij element of the reflection tensor $\Delta\varphi_{ij}^{ripples}(q,t)$ as to be summed to those considered previously (associated to both the temperature grating and the elasto-optic grating) in eq. (2.9).

We will show in subsection (2.2.2) that our measurements confirm the presence of a phase and an amplitude grating, whose induced dynamics differ.

2.2 Transient grating experimental setup

In this section we shall describe the laser sources producing the pump and probe beams of the TG experiment, and the optical set-up exploited to realize the experiment with an heterodyne detection of the signal (HD-TG) [41].

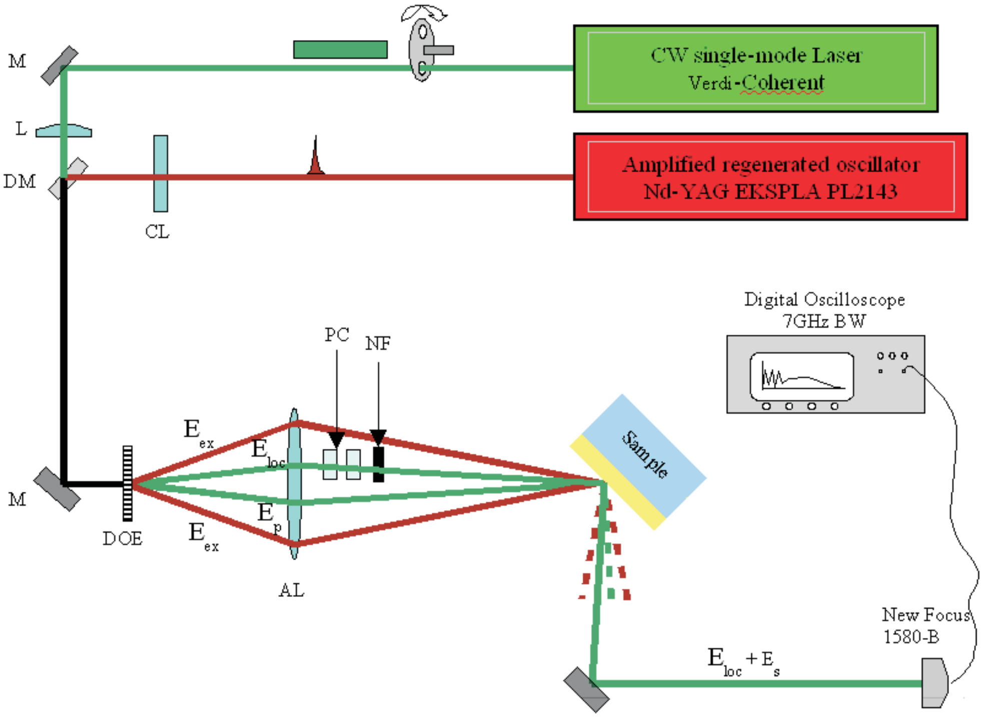

Figure 2.3: Optical set-up and laser system for the HD-TG experiment with optical heterodyne detection in reflection geometry. L: convergent lens; CL: cylindrical lens; M: mirrors; DM: dichroic mirror; DOE: diffractive optical element; AL: achromatic doublet; NF: neutral filter; PC: phase control prisms

2.2.1 Laser system and optical setup

The lasers and the optical set-up present in our laboratory are reported in Fig. 2.3. Infrared pump pulses at 1064 nm wavelength with temporal length of 20 ps and repetition of 10 Hz are produced by an amplified regenerated oscillator (Nd-YAG EKSPLA PL2143). The output pulses energy can be varied between 1 mJ and 50 mJ. The probing beam, at 532 nm wavelength, is produced by a diode-pumped intracavity-doubled Nd-YVO (Verdi-Coherent); this is a CW single-mode laser characterized by an excellent intensity stability with low and flat noise-intensity spectrum.

The two beams are collinearly coupled by the dichroic mirror DM and sent on the grating phase (DOE Diffractive Optical Element), described in detail later. This produces the two excitation pulses, E_{ex}, the probing, E_p, and the reference beam, E_l. These beams, cleaned by a spatial mask of other diffracted orders, are collected and focused on the sample's surface by an achromatic doublet (AL, $f = 160\ mm$). This optical element is mounted over a slide guide to translate along the optical axis in order to vary the magnification of the system and so the induced wave vector. In this way the excitation grating produced on the sample is an image of the enlightened DOE phase pattern whose magnification is established by the AL position [42], [43]. The local laser field is also attenuated by a neutral density filter NF and adjusted in phase by with the use of a pair of quartz prisms that allow to vary the optical path of E_l with respect to E_p, and so their relative phase (to avoid confusion please note that in Fig. 2.3, PC stand for Phase Control).

The HD-TG signal is optically filtered from eventual spurious components and measured by a fast photodiode, New Focus model 1580-B with a bandwidth of DC$-12\ GHz$. The signal is then recorded by a digital oscilloscope with a $7\ GHz$ bandwidth (at the voltage scale we work it reduces down to about $1\ GHz$) and a $20\ Gs/s$ sampling rate (Tektronix). The measured signals have a typical temporal duration of some microseconds so the time window of the oscilloscope. The sampling of the signal is the maximum allowed by the oscilloscope: $50\ ps$ time-step). Each scan is an average of 1000 recordings, which is sufficient to produce an excellent signal to noise ratio.

We reduced the laser energy on the samples to the lowest possible level to avoid undesirable thermal effects, and the CW beam has been gated in a window of about $3\ ms$ every $100\ ms$ by using a mechanical chopper synchronized with the excitation pulses. Depending on the induced wave vector, the mean exciting energy was in the range $0.4-4\ mJ$ for each pump pulse and the probing power was about

$10-100$ mW. The reference beam intensity is very low; it was experimentally set by means of a variable neutral filter in order to be almost 100 times the intensity of the diffracted signal. With these intensities, the experiment was well inside the linear response regime and no dependence of HD-TG signal shape on the intensities of the beams could be detected.

As already stated in the introduction, the diffractive optical element DOE was first introduced in 1998 [42,43]. It provides considerable advantages. It is a transmission phase grating, characterized by a square shaped profile, is hollowed out on a fused silica plate by ion beam techniques. Thanks to the square profile of the grating, it is possible to obtain very high diffraction efficiency on the only first orders by controlling the depth Δ of the grooves. Choosing $\Delta = \frac{\lambda/2}{(n-1)}$, with n the refractive index of silica, the diffraction efficiency would be, theoretically, maximized on each first order. Since we have to diffract both 1064 and 532 nm beams, a compromise must be reached. The chosen DOE is optimized for 830 nm radiation, and it gives on a single beam at first order a 12 % diffraction efficiency for the 532 nm and 38 % for the 1064 nm.

Some important features have to be emphasized. With this set-up automatic collimation of local field and diffracted field is obtained with the further advantage of a very stable phase locking between the probing and reference beam: two crucial parameters to realize heterodyne detection. The pump and probe beams are focused on the DOE following the geometry sketched in Fig. 2.4. The pump is focused by the cylindrical lens, CL, in order to have on the sample an excitation grating extended in the q-direction (about 0.05×5 mm) while the probe beam is focused through the convergent lens L to a circular spot in order to have a probing area with much smaller dimensions in the q-direction (30×30 μm).

We recall that after light absorption two counter-propagating mechanical waves

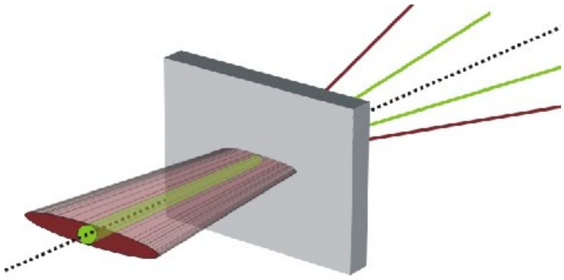

Figure 2.4: Drawing of the cylindrical spot shape of pump and the circular spot of probe on the DOE.

are launched in the q-direction and their superposition gives rise to a stationary wave. As it can be seen in Fig. 2.5 the experimental data are composed by a fast oscillating contribution (mechanical waves contribution) and a slowly relaxing term (thermal relaxation). Fourier transform of the signal allows to extract the frequency content of the excited mechanical waves in correspondence of the peaks (shown in the inset of Fig. 2.5): two different mode are excited, first is at about 280 MHz, the second at 470 MHz. Fourier transform is realized with a Fast Fourier Transform (FFT) routine. Comments over the nature of these modes are postponed to the last chapter.

What about the damping of the sound? Clearly, the two induced waves have a spatial extension in the q-direction which is limited by the dimension of the induced grating that is clearly related to the dimension of the pump pulses. Thus, the induced stationary wave has a life time due to geometrical features. This geometrical time depends on the pump spatial extension $2d$ in the q-direction and on velocity v at which the counterpropagating waves travel , i.e. on the sound phase velocity (group velocity in dispersive media) of the investigated material. In par-

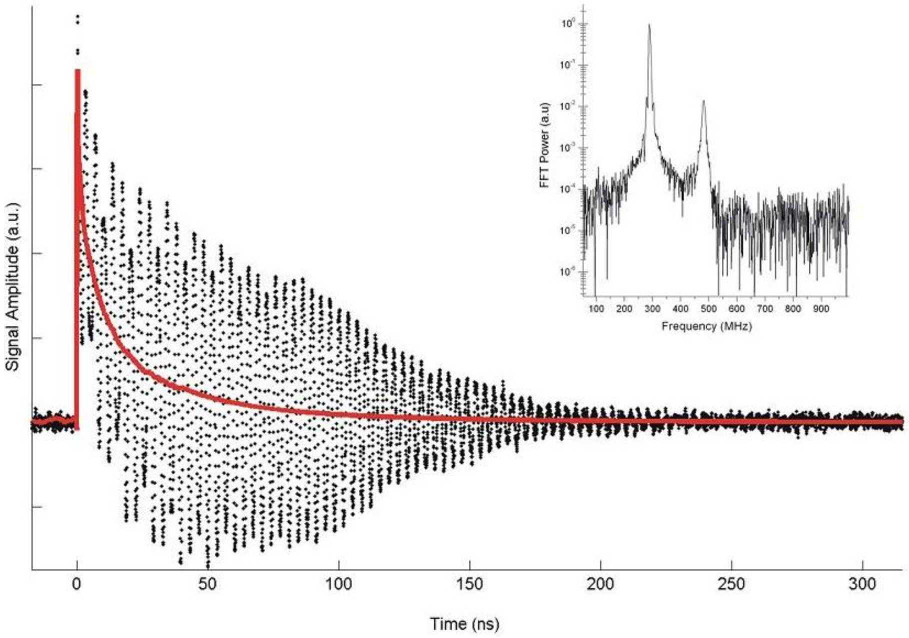

Figure 2.5: A typical HD-TG signal from a gold thin film deposited on fused silica. The signal is sampled with great accuracy every 50 ps (black points). The signal is constituted of two main contribution: a fast oscillating part and a slowly relaxing one (red line is a guide to eye). The inset shows the FFT power spectrum of the signal in semi-log scale, two modes contribute to the fast oscillating part of the signal.

ticular the transit time, or walk-off time, t given by $t = d/v$ defines the geometrical damping time. Finally, in TG experiments the natural damping time of acoustic waves is safely extracted if it is much shorter than this geometrical damping time. In fig. 2.6 we report two examples of HD-TG signals (obtained in transmission ge-

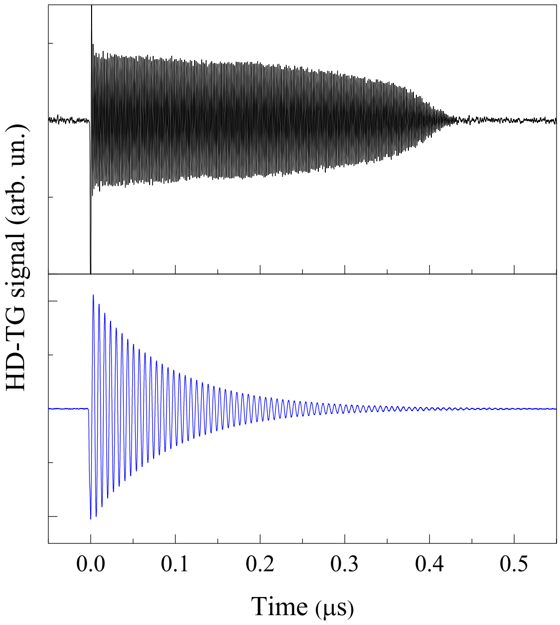

Figure 2.6: Comparison between HD-TG transmission geometry signal on fused silica (upper graph) and CCl_4 (lower graph). In the first case, the damping is dominated by the gaussian spatial shape of the pumps, whereas in the second we probe exclusively the natural damping.

ometry) where the geometrical damping and natural damping differently affect the respective signal. In the upper graph the HD-TG signal obtained for fused silica, whose natural damping time is very long compared the the geometrical: here the acoustic oscillations decay with a gaussian profile due to the pump gaussian shape. In the loweer graph, instead, we show the HD-TG signal obtained in CCl_4: here the pump width is extended enough to measure the exponential natural damping which is much shorter that in silica one. In the silica case we can observe also an other phenomenon. At around 400 ns the oscillations suddenly death. In this case the cylindrical focalization has a dimension larger than the 5 mm width of the phase mask. This dimension, considering the silica sound velocity of 6000 m/s, fixes the maximum measurable time window for the acoustic oscillation which is around 400 nm.

2.2.2 Heterodyne and Homodyne detections

Typically, detectors of electromagnetic field measure the intensity:

$$S\left(t\right)=I_s\left(t\right)=\left\langle |\mathbf{E}(t)|^2\right\rangle_{op.c.}, \tag{2.15}$$

where $\left\langle \cdot \right\rangle_{op.c.}$ means the time averaging over the optical period[1]. A direct measurement of the scattering intensity is called homodyne detection (HO). If the measured field is a signal field supplying dynamic information about some relaxing system, like in a TG experiment, through a response function $\mathcal{R}\left(t\right)$ (i.e. $E_s\left(t\right)\propto\mathcal{R}\left(t\right)$), the homodyne signal is clearly proportional to the square of the response function.

Another detection mode exists by which it is possible to directly measure the amplitude of the diffracted field; this detection mode is called optical heterodyne detection (HD). In HD, both the signal (the first order reflected diffracted field) and reference field are superimposed on the detector, and the intensity of interference field is recorded. In general $\mathbf{E}_s$ can be written as

$$\mathbf{E}_s(t)=\widehat{\mathbf{e}}\mathcal{E}_s\left(t\right)\exp\left[i\left(\mathbf{k}_s\cdot\mathbf{r}-\omega t\right)\right]+c.c., \tag{2.16}$$

with $\mathcal{E}_s(t)$, in general, a complex function; then we choose a reference field with same wave-vector, direction and frequency of $\mathbf{E}_s(t)$ and with constant amplitude $\mathbf{E}_l(t)=\widehat{\mathbf{e}}\mathcal{E}_l\exp\left[i\left(\mathbf{k}_s\cdot\mathbf{r}-\omega t+\phi\right)\right]+c.c.$, where ϕ is the optical phase between the signal and reference field and $\mathcal{E}_l$ is a real amplitude. Hence, the heterodyne signal is

$$\begin{aligned} S\left(t\right) &= \left\langle |\mathbf{E}_s(t)+\mathbf{E}_l|^2\right\rangle_{op.c.} \\ &= I_s(t)+I_l+2\{Re[\mathcal{E}_s(t)]\mathcal{E}_l\cos\phi+Im[\mathcal{E}_s(t)]\mathcal{E}_l\sin\phi\}. \end{aligned} \tag{2.17}$$

---

[1] Strictly speaking the average will be performed over the detector integration time, which even in ultrafast detectors is much longer than the time of optical cycle but generally shorter than the signal relaxation times.

The first two terms in the right-hand side of eq. 2.17 are the homodyne contribution $I_s(t) = \langle|\mathbf{E}_s(t)|^2\rangle_{op.c.}$ and the local field intensity I_l, while the third, between curly braces, is the heterodyne contribution. If the local field has a high intensity, the homodyne contribution becomes negligible and the time variation of the signal is dominated by the heterodyne term, which is directly proportional to the signal field. Moreover, this last term can be experimentally isolated by the subtraction of two signals with a phase difference of π. In fact, recording a first signal, S_+, with $\phi_+ = \ \phi_0$ and then a second one, S_-, with $\varphi_- = \phi_0 + \pi$, we immediately have

$$\begin{aligned} S^{HD}(t) &= [S_+ - S_-] \qquad (2.18) \\ &= 4\left\{Re\left[\mathcal{E}_s\left(t\right)\right]\mathcal{E}_l\cos\phi_0 + Im\left[\mathcal{E}_s\left(t\right)\right]\mathcal{E}_l\sin\phi_0\right\}. \end{aligned}$$

It is clear from expression 2.18 that by choosing $\phi_0 = 0$ or $\pi/2$, it would possible to extract only the real or imaginary part of $\mathcal{E}_s\left(t\right)$. Still the phase relation between the two field is not known in absolute but only in relative terms, so that we are not able to separate the various contributions.

In fact in a TG experiment, $Re\left[\mathcal{E}_s\left(t\right)\right]$ corresponds to a birefringence-phase grating, and $Im\left[\mathcal{E}_s\left(t\right)\right]$ corresponds to a dichroic-amplitude grating [37,44,45]. As we have demonstrated, a signal obtained from a metal film contains both the real and imaginary contribution, as indicated in eq.(2.9), that are, on their side, realized by different effects such as elasto-optic coupling, temperature grating and surface ripples. Both contributions (real and imaginary) to the signal have shown to be effective, and with different dynamics content as it can be understood from figure 2.7 where each of the 20 recorded signal is obtained at a phase ϕ_0 according to (2.18) and the phase ϕ_0 is varied of $\pi/10$ from measurement to measurement in order to cover the full phase angle 2π.

The fact that the various induced grating do not produce the same dynamics is easily understood in terms of the absence of a phase term ϕ_0 that cancels all the oscillating contribution at all times, has it should results according to (2.18) if

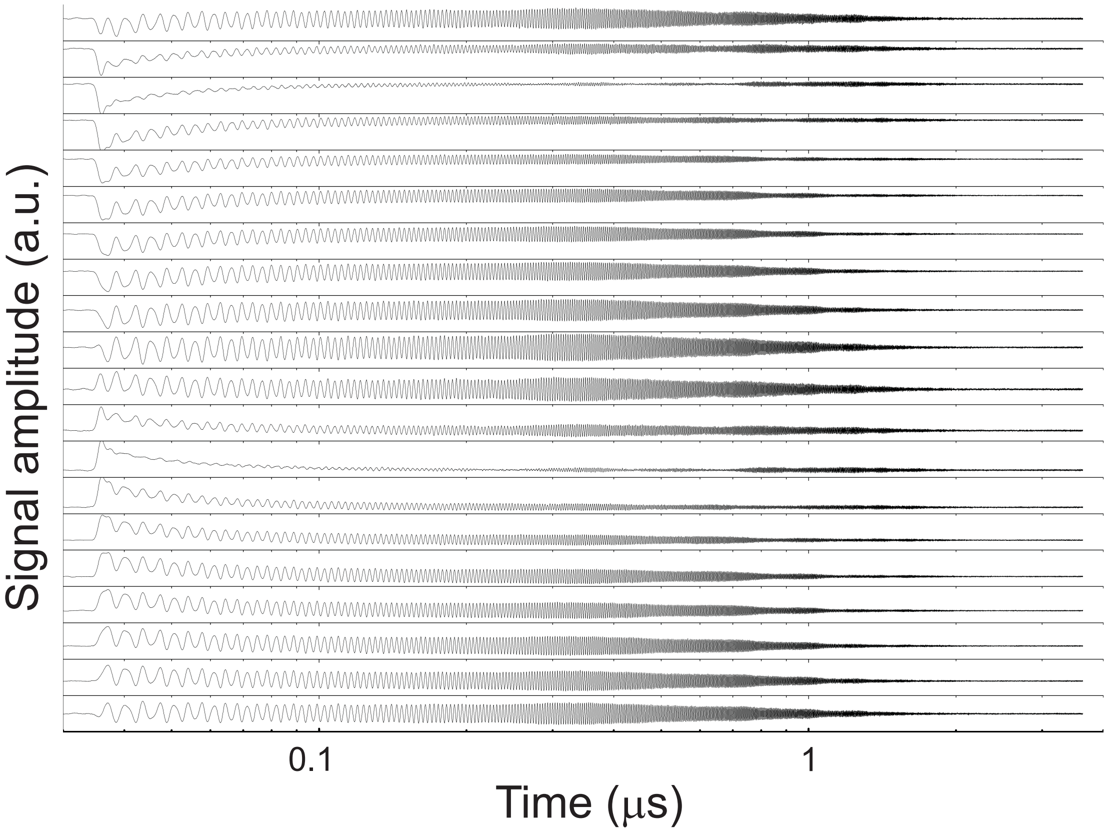

Figure 2.7: HD-TG measurements obtained at different ϕ_0 values from a sample constituted by a gold film over a fused silica substrate. No value of ϕ_0 is identified that cancels oscillatory contribution at all time. This can be explained only in terms of different dynamics arising from the various induced gratings.

both the amplitude and phase gratings would induce the same dynamics. Anyhow it has to be stressed that, the frequency content relative to measurements at different ϕ_0 is not altered in terms of frequency shift, but in terms of the amplitude of each excited mode.

It is important to emphasize the major advantages in using heterodyne instead of homodyne detection. First, it substantially improves the signal to noise ratio in the observed time window, because of both the signal increment and the cancellation of the spurious signals which are not phase sensitive. Second, it enhances the dynamic range since the recorded signal is directly proportional to signal field instead of being proportional to its square. In the study of materials with a weak scattering efficiency and complex responses, these features turn out to be of basic importance. Furthermore, HD allows the measurement of the signal at very long times, where the TG signals become very weak. Nevertheless, the effective realization of such detection is quite difficult at optical frequencies. Indeed, to get an interferometric phase stability between the diffracted and the local field is not a simple experimental task, which explains why only very few HD-TG experiments have been realized so far [37]. The introduction of the phase mask DOE in the TG optical setup (see subsection 2.2.1) has considerably reduced the difficulties of achieving heterodyne detection.

2.3 Samples

The sample that we characterized is a gold coated fused silica plate 2 mm thick. An image of the sample is shown in Fig. 2.8(a). Two distinct area are clearly distinguishable, an homogeneous region and a grooved one (5 × 5 mm). During this work we have theoretically and experimentally characterized both regions. In the rest of this thesis we will refer to those region as to the homogeneous sample and the PC sample. The grooving displayed in Fig. 2.8(b) is obtained by photolithographically defining a one dimensional squared optical grating in a layer of photoresist coated on the glass surface. Reactive ion etching enables to transfer the grating pattern to the glass surface. The remaining photoresist is then removed with acetone. Finally, in order to excite surface acoustic waves, a thin gold film is deposited on the surface by evaporation. In Fig. 2.8(c) a schematic view of the grooving is given. The parameters peculiar of the lattice are: the lattice step a=5

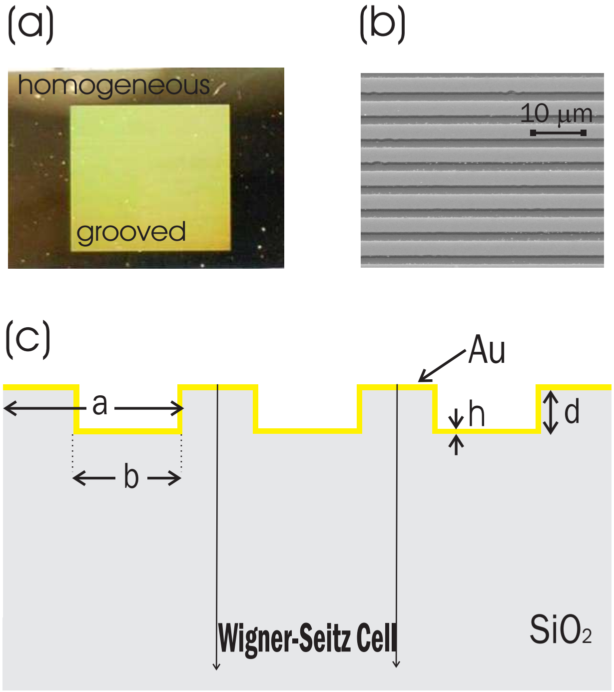

Figure 2.8: (a) Macroscopic image of the sample. Two regions are identified: the homogeneous and the grooved one. In (b) a SEM image of the grooved area and in (c) a scheme corresponding to a cross section of the sample perpendicular to the grooving.

μm, the duty cycle b/a=52%, the depth of the squared lattice d=0.860 μm and, both for the homogeneous and grooved region, the film thickness h=0.130 μm. The Wigner-Seitz cell is that chosen to simulate the band diagram of the sample itself.

The values of mechanical parameters of both medium (Young's modulus E, Poisson's ratio ν and density ρ) are plotted against a wide range of temperature in Fig. 2.9. First row is that relative to gold's parameters while second one is that of fused silica.
We can relate these mechanical parameters to those present in the equation of dynamics (1.10) (again the density ρ plus c_l and c_t, the longitudinal and transverse

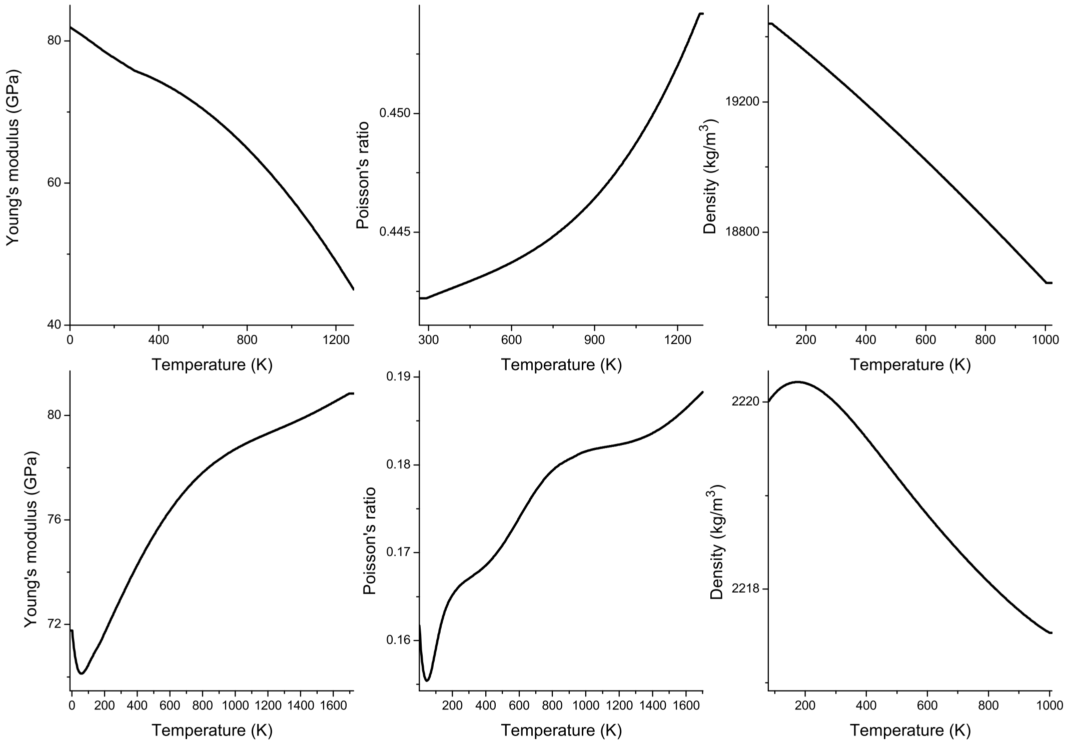

Figure 2.9: First row: gold mechanical parameters as a function of temperature over a wide range. Second row: fused silica mechanical parameters

velocity respectively) according to the following equations

$$c_l = \sqrt{\frac{1}{\rho}\frac{E(1-\nu)}{(1+\nu)(1-2\nu)}} \tag{2.19}$$

$$c_t = \sqrt{\frac{1}{\rho}\frac{E}{2(1+\nu)}} \tag{2.20}$$

We performed our measurements at room temperature, however it has to be noted that even a huge variation of 10 K around the room temperature do not significantly alters the mechanical parameters. Their values at room temperature are shown in the table underneath.

	Gold	Fused silica
Young's modulus (GPa)	75.8	72.9
Poisson's ratio	0.442	0.167
Density (Kg/m^3)	$19.3 \cdot 10^3$	$2.22 \cdot 10^3$
Transverse velocity (m/s)	$1.17 \cdot 10^3$	$3.75 \cdot 10^3$
Longitudinal velocity (m/s)	$3.62 \cdot 10^3$	$5.93 \cdot 10^3$

Chapter 3

SIMULATIONS

A consistent part of this study has been directed towards the theoretical characterization of the dispersion relation of the analyzed samples. In this chapter the main characteristics of the software by which simulations has been realized will be briefly introduced. The goodness of our simulations will be then tested in comparison with literature results [9] and a standard procedure for the eigenfrequency analysis will be given. Finally the comparison between literature's experimental TG results regarding propagation of SAW in periodic surfaces (lacking of any simulation) [29] [30] will be compared to the simulations that have been performed on those samples.

3.1 COMSOL Multiphysics ©

COMSOL Multiphysics (CM) is a commercial software. It consists of a simulation environment that allows all steps in the modelling process (defining the geometry, specifying the physics, meshing, solving and then post-processing the results) without any specific programming knowledge. It performs calculations of partial differential equations (PDE) over complex domains performing a finite element analysis (FEA). FEA is a numerical technique to find approximate solutions to PDE. The solution approach is based on transforming PDE into an approximating system of ordinary differential equations, that are numerically stable and can be solved with standard techniques.

Model set up is quick, thanks to a number of predefined modelling interfaces for applications ranging from fluid flow and heat transfer to structural mechanics (that of our interest) and electromagnetic analysis. Material properties, source terms and boundary conditions can all be arbitrary functions of the dependent variables.

COMSOL Multiphysics operates as the primary tool for modelling needs. Its main peculiarities are its versatility, flexibility and usability.

3.1.1 Structural mechanics module

This module is specialized in the analysis of components and subsystems where it is necessary to evaluate structural deformations. Application modes in this module solve stationary and dynamic models, perform eigenfrequency, parametric, quasi-static and frequency-response analysis.

COMSOL Multiphysics includes four application modes for stress analysis and general structural mechanics simulation:

- The Solid, Stress-Strain application mode (for 3D geometries)
- The Plane Stress application mode, applicable in volume bodies with one dimension much smaller than the other two (realizes a 2D geometry)
- The Plane Strain application mode, usually applied in volume bodies with one dimension (z in Fig. 3.1) much bigger than the other two (realizes a 2D geometry)
- The Axial Symmetry Stress-Strain application mode (for 2D axisymmetric geometries)

The last three cases are 2D simplifications of the full 3D equations. Simplifications are valid under certain assumptions.

3.1.1.1 Plane Strain application mode

The Plane Strain application mode solves for the global displacement (u_x, u_y) in the x and y directions. In a state of plane strain the out of plane components of the strain tensor are assumed to be zero. Plane Strain assumes that the extension (along z) of a body normal to the plane section (xy) of the analysis is of infinite length, and that the motion along this direction is not effective for that in the xy plane. Some common engineering problems such as a dam subjected to water loading, a tunnel under external pressure, a pipe under internal pressure, or a cylindrical roller bearing compressed by force in a diametral plane, have significant strain only in a plane; that is, the strain in one direction is much less than the strain in the two other orthogonal directions. If small enough, the smallest strain can be ignored and the part is said to experience plane strain.

Plane strain mode is our framework: in fact both 2D PC and 1D PC that have been analyzed within this work fall in this classification. In fact, it can be shown that, in a 2D periodic structure whose periodicity is realized in the xy plane, the vertical displacement u_z is decoupled, at least in isotropic media, from that on the xy plane and does not affect it [12]. Then, the approximation of this mode analysis (motion in z direction is not effective for that in the xy plane) is valid and applicable to the study of a 2D periodic structure. Also 1D surface periodic structures fit this application mode in fact, as it is shown in Fig. 3.2, the sketched 1D superficial periodic structure is invariant along the z direction, so that the problem regarding propagation of mechanical waves in the PC can be fully solved in the xy plane.

The application mode will perform eigenfrequency analysis in order to fully

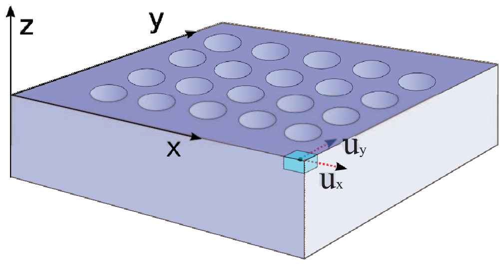

Figure 3.1: Also 2D periodic structure can be solved in the plane strain mode: along the z direction, invariant for translation, the displacement u_z is decoupled from that in the plane u_x and u_y [12].

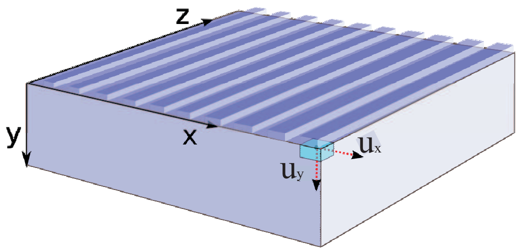

Figure 3.2: Schematic draw of a 1D superficial PC. The sample is z direction invariant. Once again the displacements u_x and u_y in the plane xy can be fully calculated independently of the z dimension.

reconstruct the band diagram of the analyzed PC.

3.2 Standard procedure and software test

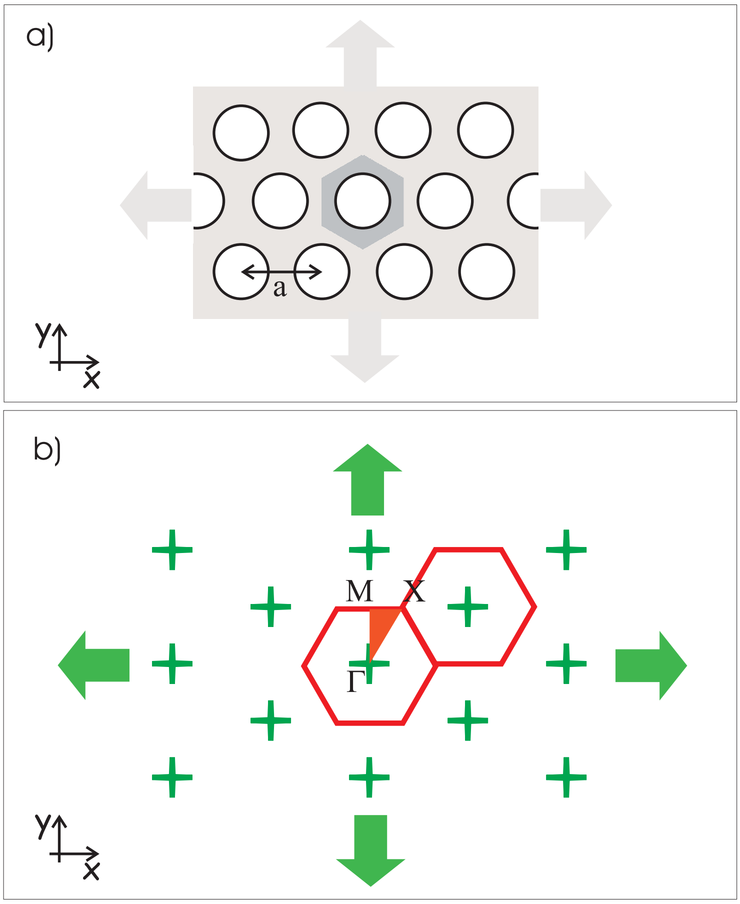

Figure 3.3: a: The direct lattice of a triangular lattice with lattice step a. The Wigner-Seitz cell (WSC) over which the simulations is realized is in dark grey. The big arrows indicate that the system extends beyond the sketch.
b: The related reciprocal lattice. The Brillouin zone is hexagonal as the WSC but rotated of $\pi/6$. The red area represents the ZIB.

In order to check the reliability of the simulations realized with CM a comparison with literature result from the paper of Gorishnyy et al. [9] has been realized.

This section is organized as follows: first the procedure to realize the simulations will be shown (the specific geometry that is presented here will be easily extendible to other general cases), then a direct comparison of the simulated band diagrams will be presented.

3.2.1 Setting up the simulation

Once that the appropriate structural mechanic module (plane stress) and application mode (eigenfrequency analysis) have been chosen it's time to concentrate on the geometry of the system. The sample investigated in [9] consists of triangular arrays of empty cylindrical holes in epoxy matrix (with a radius to lattice step ratio of 0.33) and the relation dispersion to be characterized is that of bulk waves propagating in the plane orthogonal to the cylinder axis with wave vector along the ΓM direction of the irreducible Brillouin zone (ZIB). The first step is to design the Wigner-Seitz cell of the system under study (`Draw` menu) and assign the appropriate materials to the domains trough the `Physics/Subdomain Settings` menu. Until now no prescriptions have been given to the software about the periodicity of the system. This is realized imposing the displacement field to satisfy the Bloch conditions on the boundary of the cell. In this particular case there are three translation relative to three different direct lattice vectors which define the translation from side 1 to side 4 ($R14$), side 2 to side 5 ($R25$) and side 6 to side 3 ($R63$) where side 1 is chosen to be vertical side on the left and enumeration proceeds clockwise.

How this informations are given to the software? This is realized substantially in two steps. The first one consists in defining the opportune constants trough `Options/Constants` menu (as in Fig. 3.5). The second is realized imposing the Bloch conditions trough the `Physics/Periodic Boundary Conditions` menu. Here side i is selected (be it 1, 2 or 6) and two constraints are defined: horizontal dis-

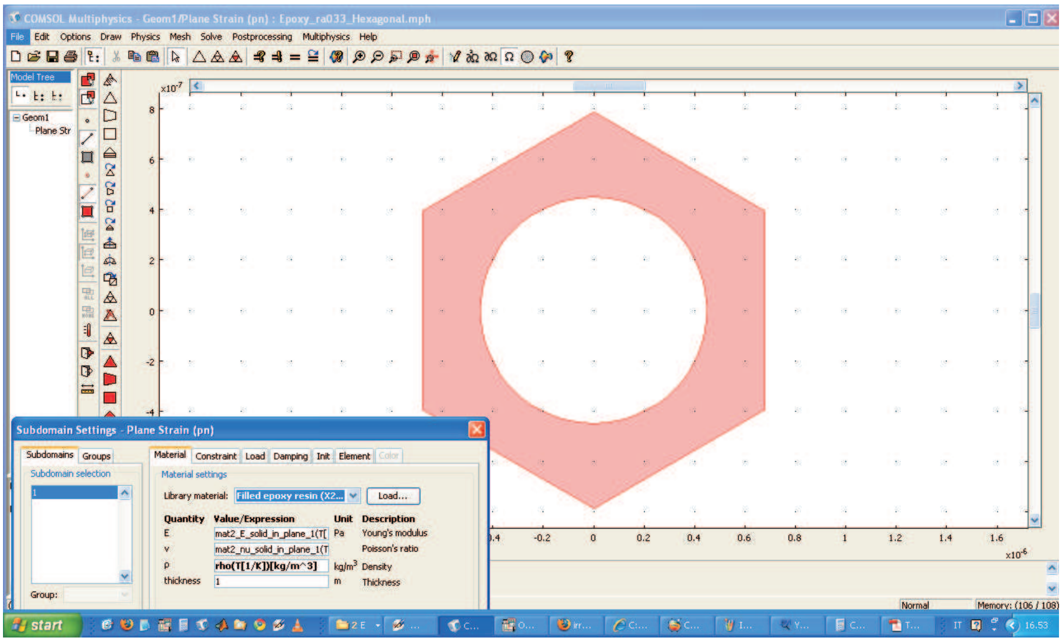

Subdomain Settings - Plane Strain (pn)

Subdomains | Groups | Material | Constraint | Load | Damping | Init | Element | Color

Subdomain selection: 1

Group:

Material settings

Library material: Filled epoxy resin (X2...

Load...

Quantity	Value/Expression	Unit	Description
E	mat2_E_solid_in_plane_1(T[	Pa	Young's modulus
ν	mat2_nu_solid_in_plane_1(T		Poisson's ratio
ρ	rho(T[1/K])[kg/m^3]	kg/m³	Density
thickness	1	m	Thickness

Figure 3.4: Draw of the WSC and subdomain material selection.

placement u_x^i and vertical displacement u_y^i (which are internal software variables). Then the opposite side j (4, 5 or 3 respectively) is given as destination for the defined constraints with the requirement that here displacement differ in phase according to Bloch theorem:

$$u_x^j = u_x^i \cdot e^{i \cdot (k_x \cdot Rij_x + k_y \cdot Rij_y)} \tag{3.1}$$

$$u_y^j = u_y^i \cdot e^{i \cdot (k_x \cdot Rij_x + k_y \cdot Rij_y)} \tag{3.2}$$

Once that this constraints are passed to the software the solution (eigenvalues and corresponding displacement field) will be, by definition, that proper of an infinite periodic system, exactly the PC. Introducing the geometrical and elastic parameters of the sample, specified in [9] the CM program is ready to run which is done by the `Solve/Solve Problem` menu. This automatically meshes the domains and calculates the eigenvalues of the system. Setting the desired number of eigenmodes to n the software will determine the first n eigenmodes which fulfill the defined

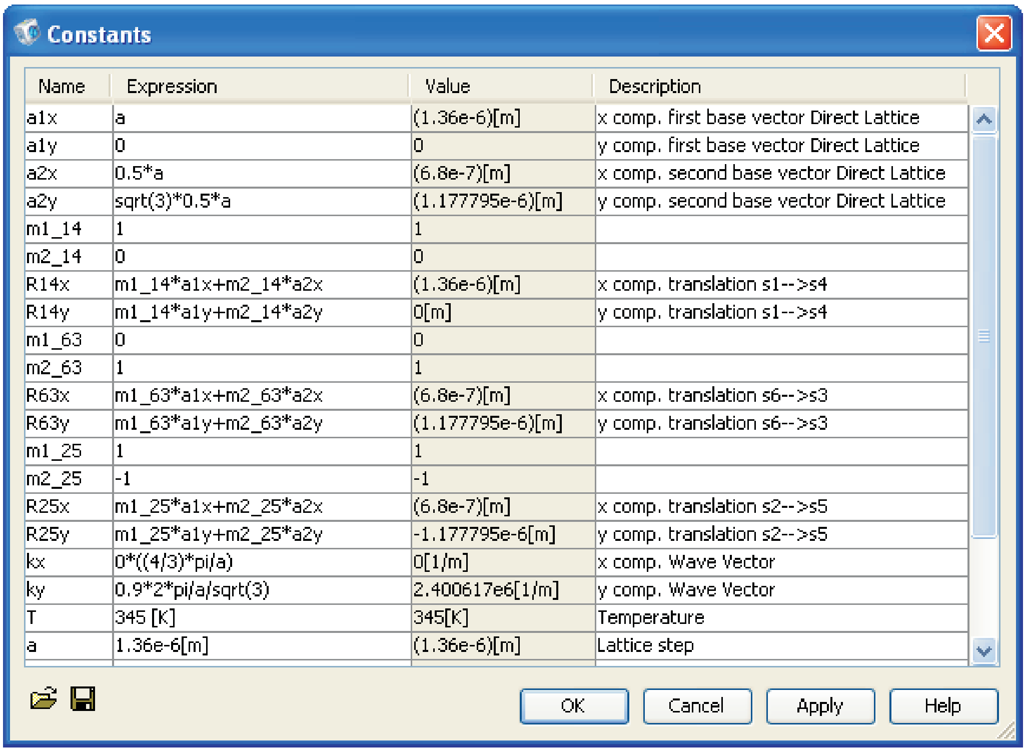

Name	Expression	Value	Description
a1x	a	(1.36e-6)[m]	x comp. first base vector Direct Lattice
a1y	0	0	y comp. first base vector Direct Lattice
a2x	0.5*a	(6.8e-7)[m]	x comp. second base vector Direct Lattice
a2y	sqrt(3)*0.5*a	(1.177795e-6)[m]	y comp. second base vector Direct Lattice
m1_14	1	1	
m2_14	0	0	
R14x	m1_14*a1x+m2_14*a2x	(1.36e-6)[m]	x comp. translation s1-->s4
R14y	m1_14*a1y+m2_14*a2y	0[m]	y comp. translation s1-->s4
m1_63	0	0	
m2_63	1	1	
R63x	m1_63*a1x+m2_63*a2x	(6.8e-7)[m]	x comp. translation s6-->s3
R63y	m1_63*a1y+m2_63*a2y	(1.177795e-6)[m]	y comp. translation s6-->s3
m1_25	1	1	
m2_25	-1	-1	
R25x	m1_25*a1x+m2_25*a2x	(6.8e-7)[m]	x comp. translation s2-->s5
R25y	m1_25*a1y+m2_25*a2y	-1.177795e-6[m]	y comp. translation s2-->s5
kx	0*((4/3)*pi/a)	0[1/m]	x comp. Wave Vector
ky	0.9*2*pi/a/sqrt(3)	2.400617e6[1/m]	y comp. Wave Vector
T	345 [K]	345[K]	Temperature
a	1.36e-6[m]	(1.36e-6)[m]	Lattice step

Figure 3.5: List of the constants defined by the user.

sample from the lower eigenfrequency mode. The CM program solves the equation of motion defining the eigenvalues and eigenvectors. The relative displacement field are shown on the main prompt, ready to be postprocessed. Varying the wave vector k_y specified in the constants the relation dispersion over ΓM is obtained. However, defining the appropriate wave vector in the constants, it is possible to fully characterize the relation dispersion along all the boundaries of the ZIB as it can be understood from Fig. 3.3 b. For example if interested in the dispersion along ΓX it is sufficient to set k_y=0 in the constants and vary the value of k_x from zero up to $\|\Gamma\mathrm{X}\| = 4\pi/3a$ with convenient stepping. Finally to investigate the XM edge k_x will be varied (keeping k_y=0) between $\|\Gamma\mathrm{X}\|$ and $\|\Gamma\mathrm{X}\|+\|\mathrm{XM}\|$ with the opportune stepping.

Finally, before comparing CM simulated band diagram with literature, it is worth

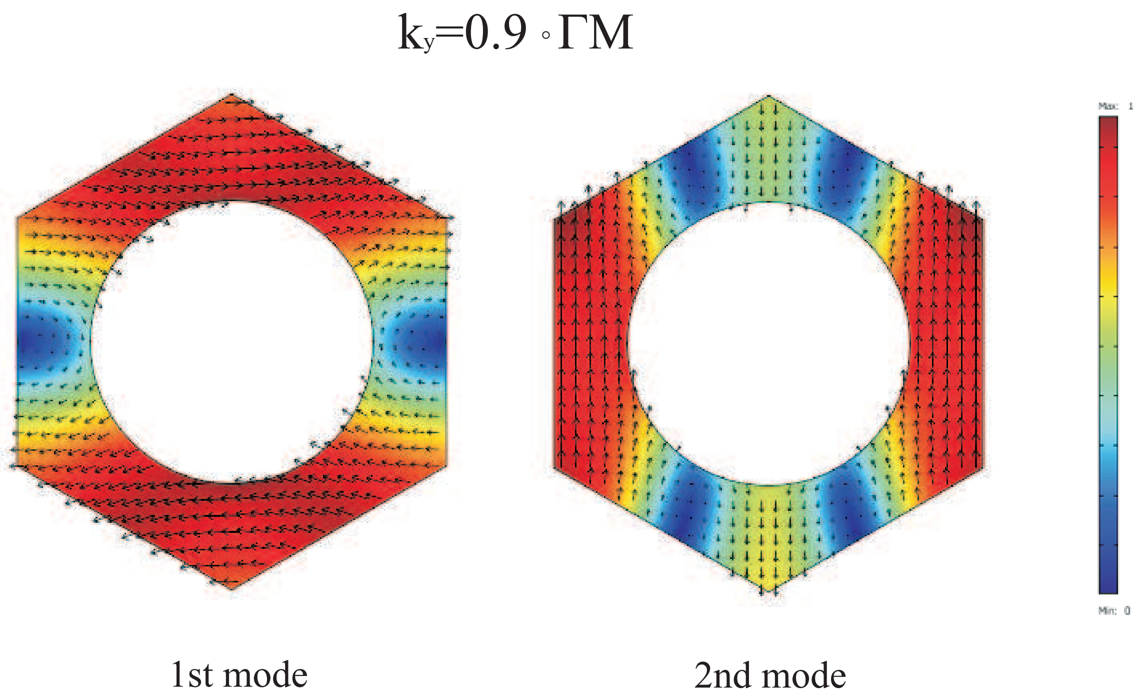

Figure 3.6: Displacement field associated to the first (predominantly transverse) and second (predominantly longitudinal) eigenmode. Colour scale represents the total displacement ($\sqrt{u_x^2 + u_y^2}$) in arbitrary units. Arrows stand for the displacement field (also in arbitrary units).

noticing that plotted arrows in the first mode of Fig. 3.6 clearly manifest the predominantly transverse character of this eigenmode (remember wave vector is along y axis, vertical direction in figure), while, the second one is predominantly longitudinal.

3.2.2 The comparison with literature

In Fig. 3.7 a comparison with some literature results is presented. The band diagram characterized in [9], has been simulated by CM and compared with that reported in [9]. Data from [9] are represented by open circles in Fig. 3.7, blue (green) circles correspond to mainly transverse (longitudinal) modes, as stated in

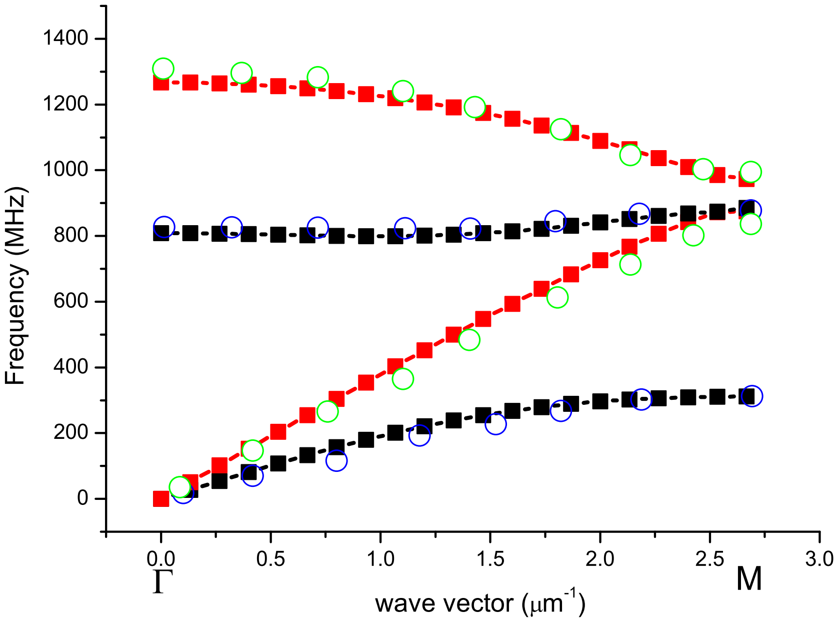

Figure 3.7: Comparison between band diagram present in [9] (open circles) and CM simulations (dashed squares). Different colours within the same set of simulations correspond to different states of polarization of the modes (see text).

the paper. The simulation realized with CM program using the previously reported procedures is plotted with full dashed squares. Black (red) squares correspond to mainly transverse (longitudinal) modes.

It has to be stressed that the agreement between our simulation and the data from [9] is really satisfying. This staten, CM reveals itself as a reliable software to perform such calculations and modelings. This has proven to be a fundamental and innovative part of this Ph.D. thesis, since, to our knowledge, no scientific publications declaring the employment of this software were present when we started to use it.

3.3 Periodic surfaces and CM simulations: comparison with experimental results

Some general comments over SAW have been given previously 1.2.2. This section is devoted to the simulation of two samples characterized by a periodic modulation of the surface, whose experimental analysis was realized with TG experimental technique in papers [29], [30]. In these papers theoretical characterization are missing.

In what follows the CM simulation procedure for a generic periodic surface sample is given along with a mode surface coefficient, useful to rapidly extract the superficial eigenmodes from those of the bulk material. Finally the CM calculated band structure for each of the samples investigated in [29], [30] will be compared to experimental results.

3.3.1 SAW simulations and surface mode coefficient Δ

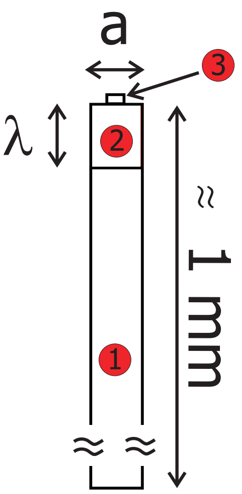

Figure 3.8: Sketch of a possible WSC for a generic 1D surface periodic samples. Three areas indicated by numbers correspond to different subdomains (not necessarily of different material) which allow for surface mode coefficient calculation.

The simulation of a thick sample presenting a surface periodicity, as that shown in Fig. 3.2 follows the same general procedure already presented. In such samples we are mainly interested in the investigation of surface waves characteristics. Some remarks are needed to make the scenario clearer.
The generic sample that we consider is a thick plate (say of a millimeter) with a 1D surface periodicity (some microns) realized on one of the two principal faces of the plate itself. Here we are defining a generic sample structure that characterize all the samples investigated in this thesis. As we will show, the simulation of the real sample will require some modification of this generic structure.
The first step consists in the definition of the cross section of minimum periodicity and the realization with CM `Draw` menu of the chosen WSC (whose choice is obviously not unambiguous). In Fig. 3.8 we report a possible WSC for a generic surface periodic sample: the vertical side is the thickness dimension of the plate , while horizontal side correspond to the lattice step of the sample itself. Once that the WSC is realized it is useful to define a depth limit from the profiled surface of about λ (remembering the constants table defined in section 3.6, this means $2\pi/\mathrm{k}_x$ since the wave vector is parallel to the surface) that identifies a surface portion of the thick plate. Then three domains can be identified within the WSC: 1 - deep bulk, 2 - superficial bulk and 3- surface. After that the integral $int_i = \iint_{D_i} \rho(\sqrt{u_x^2 + u_y^2}) dx\, dy$ should be defined (by the `Options/Integration Coupling Variables` menu) in each of the subdomains (with $1 < i < 3$) in order to properly weight the displacement associated to each domain. By means of this integrals we define the surface mode coefficient given by $\Delta = (int_2 + int_3)/(int_1 + int_2 + int_3)$. Only surface acoustic modes will have significantly non zero value of this coefficient, so that plotting Δ against the eigenmode number (remember that CM determines n eigenvalues as specified by the user) will allow to immediately identify surface eigenmodes from those of the bulk, instead of identifying them

plot after plot.

3.3.2 Periodically surface profiled homogeneous sample

The surface profiled sample that has been investigated in [29] is that shown in Fig. 3.9 (a), (b). Substantially it consists of a silica plate with square-wave surface profile, with an additional aluminum coating.

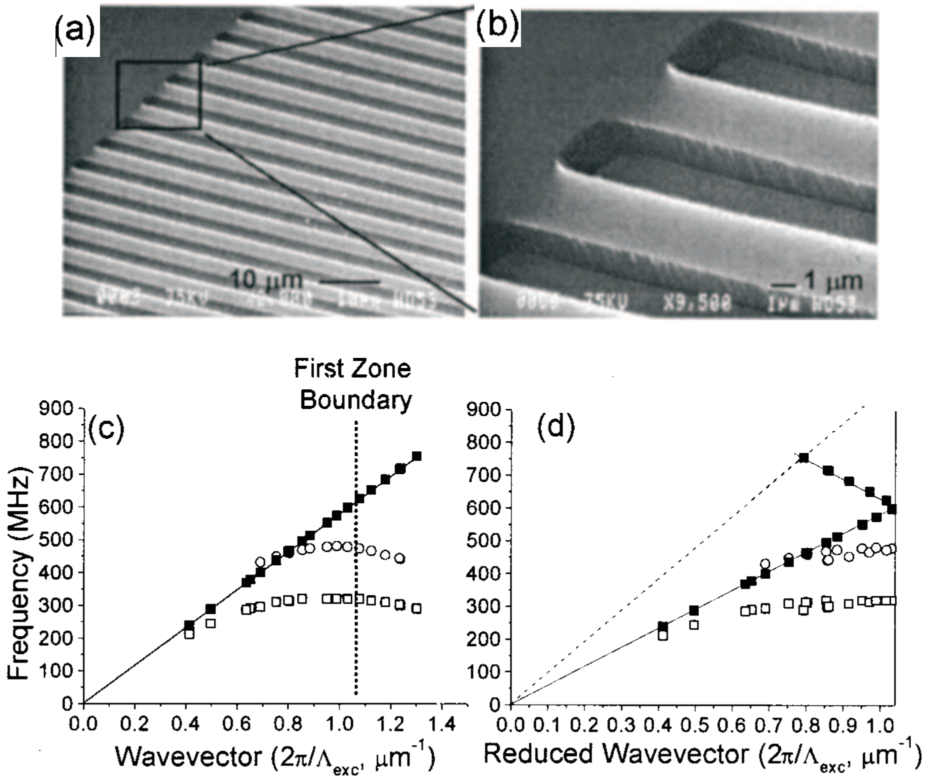

Figure 3.9: (a,b) SEM images of the surface profiled sample. The grating period is 3μm, the depth 1.15μm. An aluminum film coating of 75 nm was deposited on the sample surface to easily excite and detect SAW. (c,d) Dispersion of acoustic frequencies on the aluminum coated patterned (open symbols) and unpatterned (closed symbols) surface of glass. Vertical dotted line in (c) represents the band edge wave vector, while dashed line in (d) represents the longitudinal bulk velocity.

These measurements lack of any simulation, we have then approached the problem with CM, realizing the sample's WSC with the parameter given in [29]. Here we show that the measured experimental data can be addressed to two acoustic (in that their frequency tend to zero as wave vector goes to zero) modes of different character. The first one is the fundamental Rayleigh mode and the second is the first order Sezawa mode (will be back on this when our sample will be considered). Simulations are in agreement with the measured dispersion as can be observed in Fig. 3.10

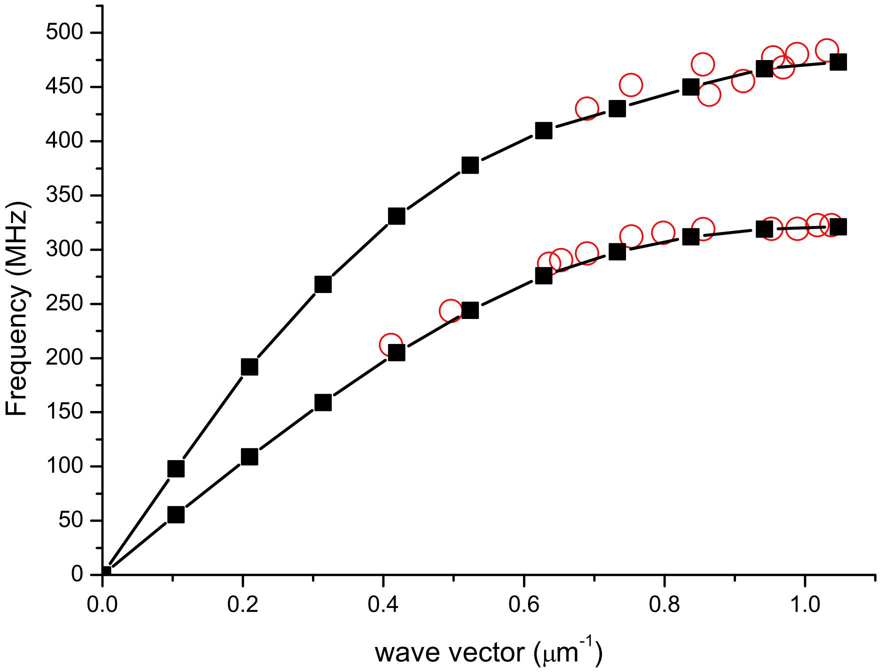

Figure 3.10: Comparison between CM realized simulations (black squares plus line) and experimental data (red circles) from [29].

3.3.3 Periodic surface elastic composites sample

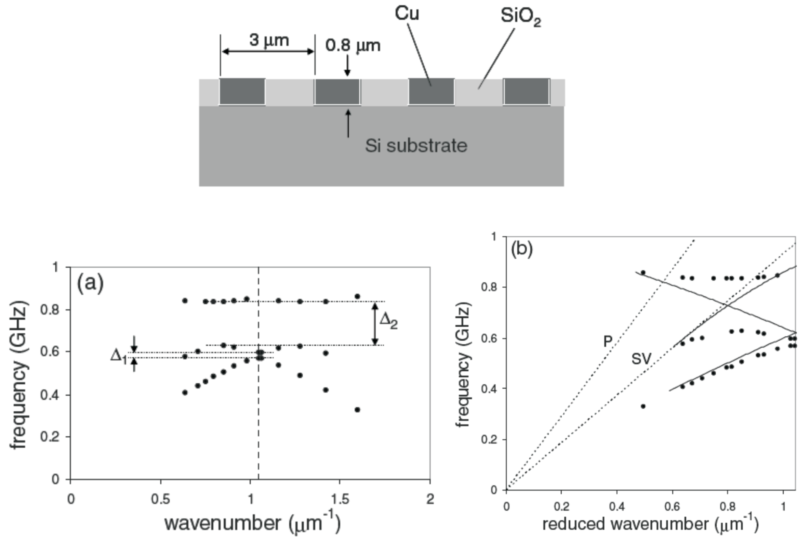

Figure 3.11: Top figure: a sketch of the sample from reference [30], and all characteristic parameters. Bottom figure: (a) measured dispersion as a function of induced wave vector, (b) dispersion as a function of reduced wave vector.

The surface composites sample of reference [30] consists of a periodic superficial arrangement of silica and copper lines over a silicon bulk, as in Fig. 3.11. This sample's periodicity is realized by alternating materials of different elastic properties, while in that of reference [29] the periodicity was determined by surface profiling. No theoretical band calculation is present in paper [30], then CM simulations have been realized, realizing the appropriate WSC in accordance with the parameters given in [30], and can be seen in Fig. 3.12. The agreement between the experimental and simulated data is really satisfying. Three modes are observed. While the first two have an acoustic character (once again in that frequency goes to zero as wave vector goes to zero), contrarily the third mode does not reach zero frequency for low wave vectors and is a flat "optical" mode (we name it "optical" in analogy with diatomic chain). Finally it can be of interest to have a look at the displacement field at the band edge (where the wavelength is twice the lattice

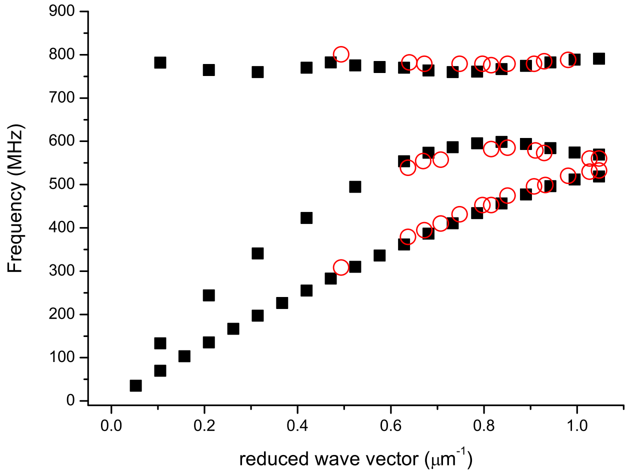

Figure 3.12: Measured (open circles) and simulated (closed squares) dispersion curves.

constant; this is the reason for we plot two adjacent WSC: an entire wavelength is appreciated). In top part of Fig. 3.13 horizontal (vertical, total) displacement u_x (u_y, $\sqrt{u_x^2 + u_y^2}$) at the very surface is shown in black (red, blue). In bottom part the displacement field plot from CM.

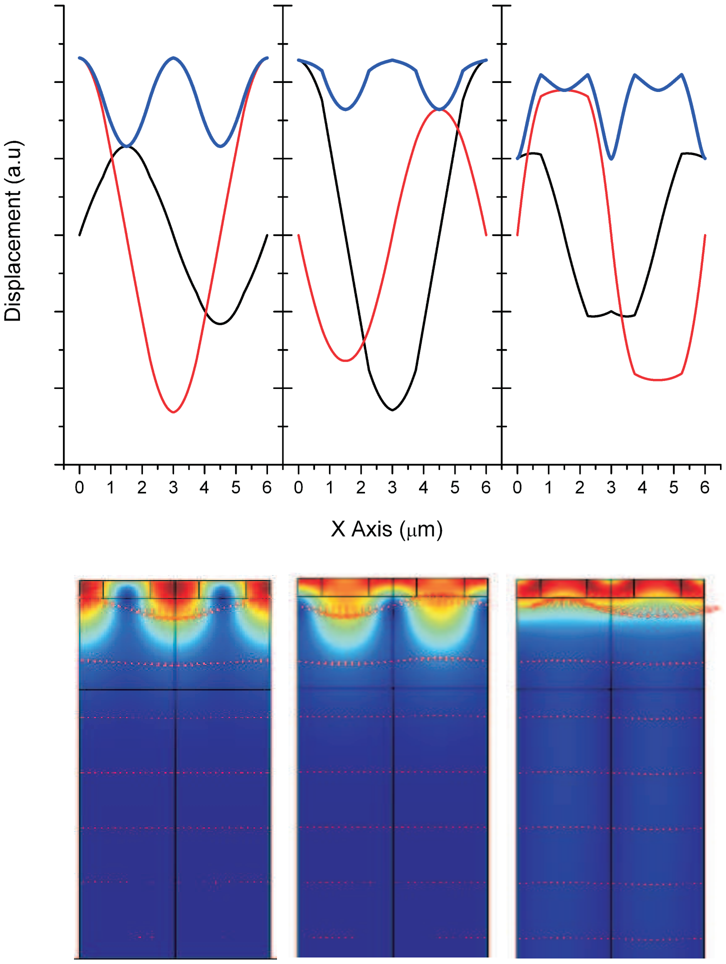

Figure 3.13: Top: displacement at the very surface of the sample for the band edge wave vector as a function of horizontal axis. From left to right: the first, second and third order mode. Black line (red, blue) correspond to u_x (u_y, $\sqrt{u_x^2 + u_y^2}$). Bottom: plot from CM for each of the simulated mode. Colour scale is for total displacement while arrows are displacement field.

Chapter 4

RESULTS AND DISCUSSION

This concluding chapter concerns the main results obtained within this Ph.D. thesis.

The results obtained both for the patterned and homogeneous region of the sample will be presented. We will mainly focus on the great difference in the measured dispersion relation between the two cases, and, in particular, great attention will be devoted to the band diagram structure revealed and theoretically calculated for the patterned region of the analyzed sample. Along with these main results other results will be presented, such as the direct measurement of extraordinary slow waves due to the surface profiling. During the discussion some key points (already widely discussed in the preceding chapters) needed for a full comprehension will be recalled.

4.1 Propagation in homogenous region and in grooved region parallel to the grooves

Subject of our study are those surface waves which lay in the sagittal plane, by definition that which contains both the normal to the surface and the wave vector.

As it has been discussed in the first chapter, the principal sagittal wave propagating at the surface of a semi-infinite media is the Rayleigh wave. This is a non dispersive and localized wave since the amplitude of its displacement decay "rapidly" in depth of the media, with a decay constant whose order of magnitude is its wavelength. As already seen in section 1.2.2 the presence of a film bounded to the substrate's surface deeply influences the propagation of SAW giving rise to many dispersive guided modes. The lower frequency mode (or first order mode, where enumeration starts from lower to higher frequencies) of these is the Rayleigh mode. In the case of a "slow" film on a "fast" substrate its velocity c_R will be comprised between the substrate's Rayleigh velocity c_{R_s} and the film's Rayleigh velocity c_{R_f} (with $c_R \rightarrow c_{R_s}$ for $qh \rightarrow 0$). Higher order modes are generally referred to as Sezawa modes and their cutoff velocity is the bulk transverse velocity of the substrate c_{t_s} for $qh \rightarrow 0$.

The dispersion relation experimentally measured on the unpatterned region of the sample is shown in Fig. 4.1 with empty circles, where the experimentally measured frequencies (obtained as the peaks values of the temporal signal FFT, as that shown in Fig. 2.5 of section 2.2.1) is plotted against the TG induced wave vector q. Two modes are evident. The continuous coloured lines correspond to the frequency obtained by the CM simulations. The experimental data and the simulated data are in optimum agreement.

Red circles correspond to the fundamental mode (the Rayleigh mode or first order mode). Consistently with the preceding considerations and that of section 1.2.2 the dependance of the frequency f on the wave vector is not linear. The phase velocity corresponding to the lower induced wave vector is $c_R = 3290 m/s$: substantially the Rayleigh velocity of the substrate since it results $qh = 0.012$ only (according to the empirical formula of eq. (1.11) the Rayleigh wave velocity of the

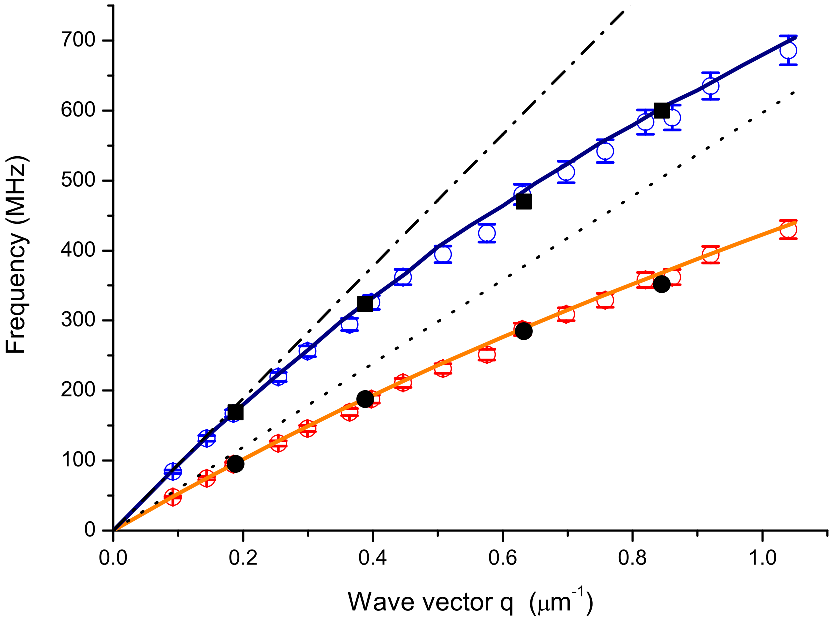

Figure 4.1: Measured and simulated dispersion of surface modes. Empty circles and full black symbols correspond to experimental measured frequency of surface acoustic modes in homogeneous region and in grooved region (with wave vector parallel to grooves) respectively. Red empty circles (full black circles) represent the Rayleigh mode, blue empty circles (black full squares) correspond to first Sezawa mode (or second order mode) which, in this wave vector range, is a pseudo-SAW. Orange and blue continuous lines correspond to simulations. Black dotted (dashed) line corresponds to the transverse (longitudinal) mode of the substrate.

fused silica substrate results $c_{R_s} = 3390 m/s$). In fact: at this value the wavelength is much bigger than the film thickness so that the wave is substantially unaffected by the gold film presence. As much as the product qh grows the wave is more and more influenced by the gold film (characterized by a much slower Rayleigh wave: $c_{R_f} = 1110 m/s$) and slows down. The phase velocity ($c = 2\pi f/q$) corresponding to the higher experimental value of the induced wave vector (at which $qh = 0.14$) is $c_R = 2600\text{m/s}$.

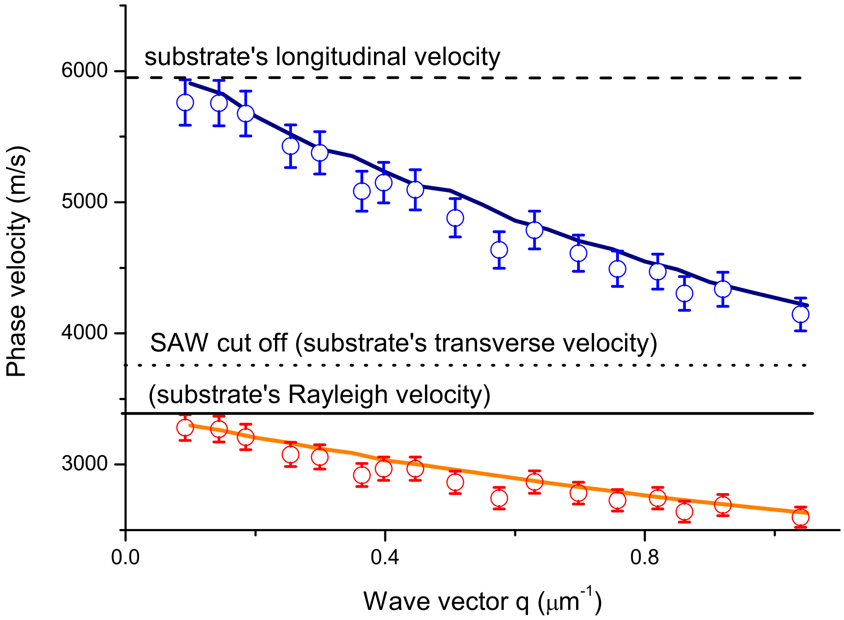

Figure 4.2: Red (blue) circles are experimental phase velocities corresponding to the first and second detected order mode. Continuous coloured lines are phase velocities obtained from the simulations. Black horizontal continuous line corresponds to the value of c_{R_s}, black horizontal dotted line corresponds to the value of c_{t_s} and black horizontal dashed line corresponds to the value of c_{l_s} (longitudinal bulk velocity of the substrate).

Also blue circles (first order Sezawa mode, or simply second order mode) have a dispersive behaviour, but, differently to red circles, do not satisfy the conditions previously stated for SAWs, as it can be seen clearly in Fig. 4.2. In fact they lay beyond the cutoff for SAW represented by the the straight dotted line (transverse velocity of the substrate c_{t_s}).

Still this cutoff is not a real physical limit in fact surface acoustic modes can exist also beyond this. This waves are known in literature as pseudosurface acoustic waves (PSAW) or leaky waves in that they radiate energy to the substrate [46,47]. The nature of these PSAW differs from that under the cutoff. As a matter of fact the displacement field and modulus has a different behaviour from those of "pure" SAWs (under the cutoff) as it will be shown in the following. The only physical cut off is given by the segmented straight line representing the substrate's longitudinal mode. We observe that for low q values the phase velocity is approximately that of the longitudinal acoustic mode in the bulk of the substrate as from Fig. 4.2.

How do these modes look like? The simulation allow us to visualize the displacement field of each mode, and this turns to be an optimum tool to have a deeper insight over the character of the surface modes. Let's make some general

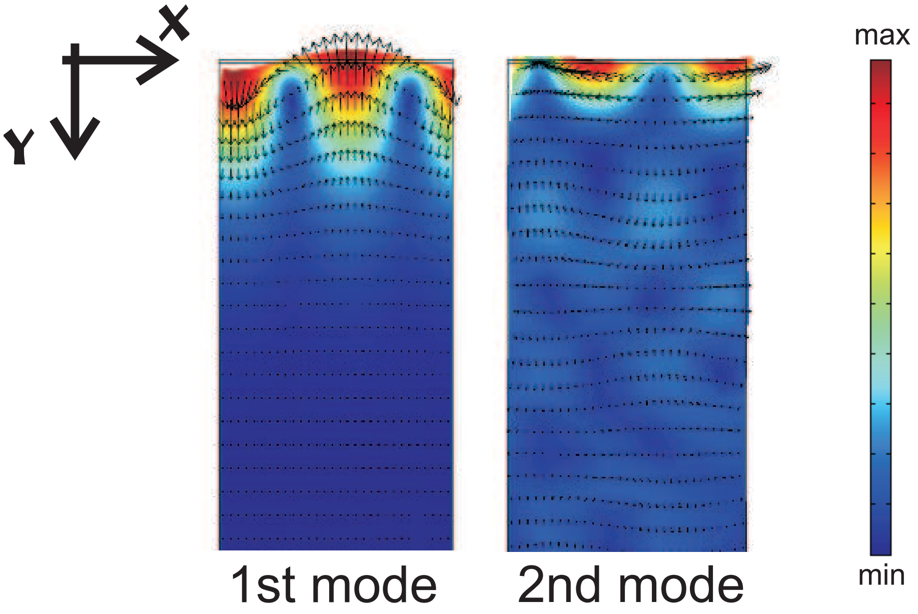

Figure 4.3: Displacement field (a.u.) associated to first and second mode is vectorially represented by the arrows, total displacement is in colour scale (legend shown on the right). The x dimension is equal to that of the simulated wavelength ($\lambda = 10\mu m \rightarrow q = 0.628\mu m^{-1}$).

comments over the two modes displayed in Fig. 4.3 (what follow holds for all the investigated wave vector range), where, arrows represent the displacement field in vectorial form, and total displacement is shown in colour scale. The x direction extension shown in the figure is equal to that of the simulated wavelength (in this particular case $\lambda = 10\mu m$). First of all: total displacement ($\sqrt{u_x^2 + u_y^2}$) clarifies the surface character of these modes, in fact the maxima are located at the very surface of the simulated sample. Another information is retrieved by means of the total displacement: the different decay in depth of the two modes. Plotting the decay of u_x, u_y and $\sqrt{u_x^2 + u_y^2}$ as a function of depth in the material (Fig. 4.4) the different behaviour of the two surface modes is evident. The first mode de-

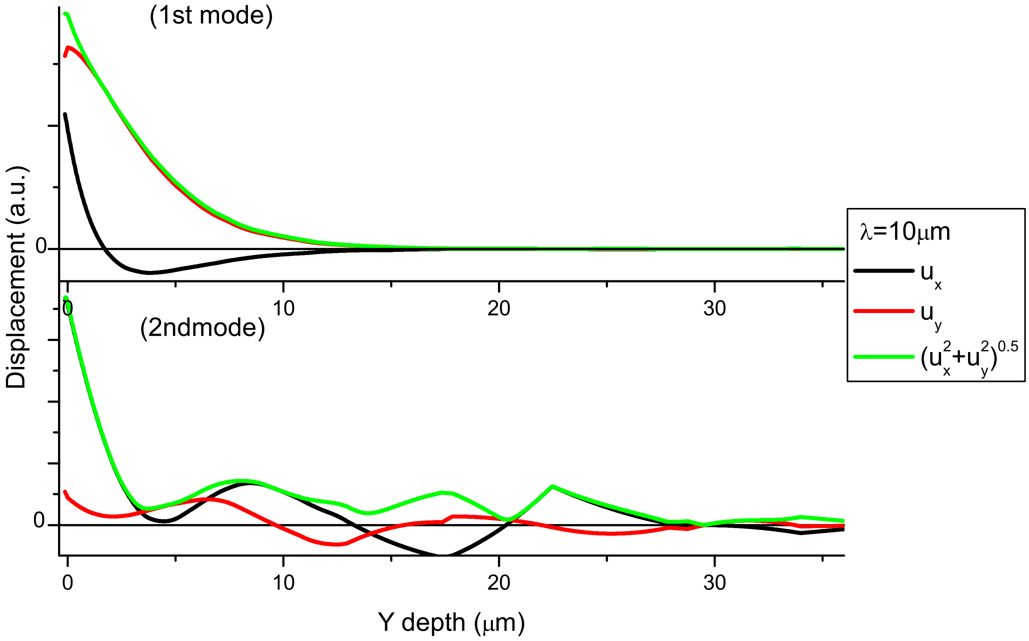

Figure 4.4: Displacement u_x, u_y and total displacement $\sqrt{u_x^2 + u_y^2}$ as a function of depth.

cays within a depth $y \sim \lambda$ and is already approximately zero when $y \sim 2\lambda$. This behaviour is that typical of SAW. The second order mode is characterized by a fast initial decay $y < \lambda/2$ that is then followed by an oscillating behaviour around a value that is not null even at a depth $y \sim 3\lambda$. That is typical of leaky waves (PSAW) where the superficial character of the waves is coupled to bulk waves, resulting in the radiation of energy (and than the associated motion) into the bulk. Another important feature that characterize the two modes is that of the ratio $max(u_y)/max(u_x)$. As it is evident both from Fig. 4.4 and Fig. 4.5 the ratio between vertical and horizontal displacement is $max(u_y)/max(u_x) > 1$ for the SAW (1st mode), and $max(u_y)/max(u_x) < 1$ for the second order mode, a PSAW. That means that the polarization associated to the surface mode is, in the first

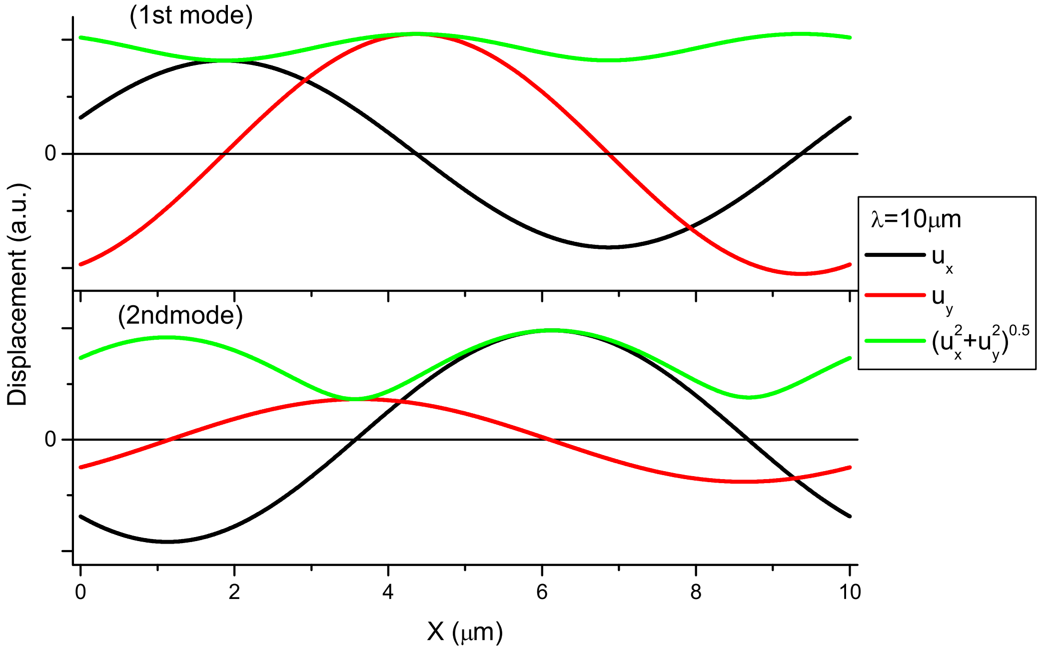

Figure 4.5: Displacement u_x, u_y and total displacement $\sqrt{u_x^2 + u_y^2}$ as a function of x.

case, that of an ellipsis with main axes along the normal to the surface, while in the second case is that of an ellipsis with main axis along the x axis, that of the wave vector associated to the modes. So, for the first mode the motion is mainly transverse, and for the second is mainly of longitudinal character, as it is evident considering Fig. 4.3.

Finally we want to underline that in both cases (first and second order mode), both displacements (u_x and u_y) evolution along the x direction (Fig. 4.5) are sinusoidal and have a relative phase difference of $\pi/2$.

The elusive nature of PSAW requires an excellent signal to noise ratio in order to detect them experimentally, in fact as one of main contribution to the signal of TG experiment is associated to the vertical displacement whereas their associated displacement is predominantly longitudinal (horizontal displacement u_x) the detection of such waves can be a hard task.

It is interesting to define a SAW likeness coefficient $\alpha = \int \int_0^{2\pi/q} v^2/u^2 dxdy$ for these PSAW (leaky waves): in Fig. 4.6 (top) it can be observed that as the wave vector increases the value of α also raises which implies that the wave tends to assume the mainly vertical character of those modes under the cutoff. This trend has an experimental confirmation as shown in Fig. 4.6 (bottom), in fact, given the predominantly vertical displacement's sensitivity of the experiment, by comparing the amplitude of the PSAW peak relative to q=0.092 μm^{-1} (in black) and to q=1.04 μm^{-1}. As expected the intensity of this peak (each spectra has been normalized so that the maximum of the first order peak is unity) is higher for the bigger wave vector, which is consistent with the observation over α.

Finally it is worth noticing that it is not surprising that we observe one only "pure" SAW in fact the qh range we explore is really narrow and close to zero $0.012 < qh < 0.14$ (dashed region shown in Fig. 4.7), which is the analogue of

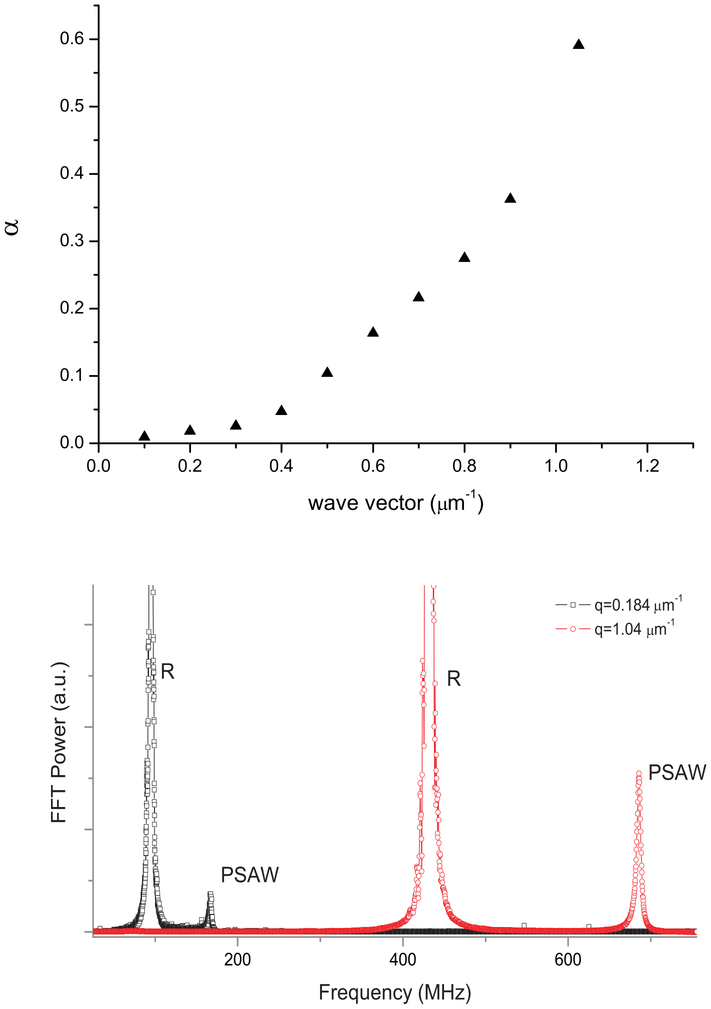

Figure 4.6: Top: SAW likeness coefficient as a function of the wave vector. Bottom: Power FFT of the signal at two different induced wave vector (each spectra has the maximum of the Rayleigh peak normalized).

Fig. 1.7 presented in section 1.2.2.

We have then induced waves on the patterned region with wave vector parallel to the grooves and, as we expected, haven't revealed any change in the relation

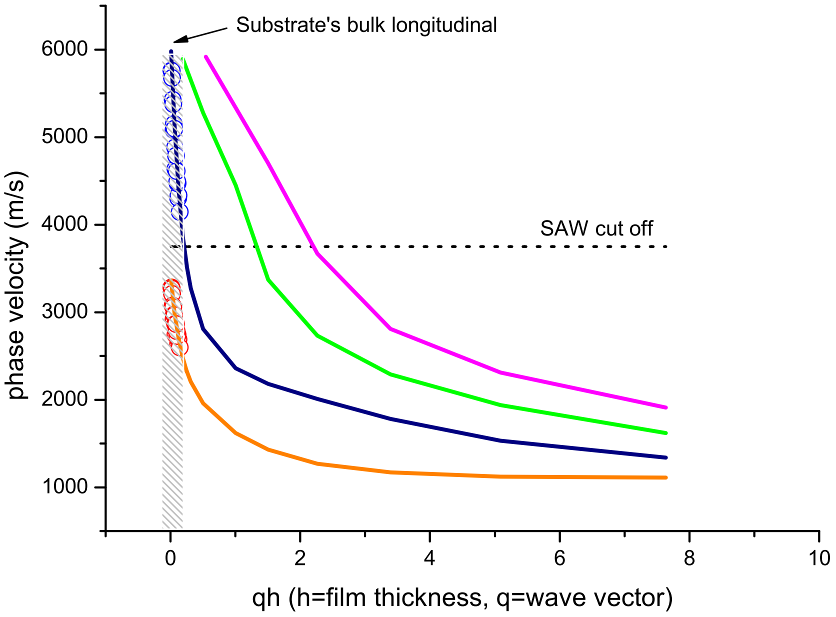

Figure 4.7: Phase velocity as a function of the product of the wave vector q and the film thickness h, experimental data are represented with circles, simulations are shown as continuous line. Shaded region is the experimentally explored region.

dispersion (see Fig. 4.1) of the two modes (black circles and square respectively): the wave do not sense the surface structure as long as it propagates parallel to grooves since, being contained in the sagittal plane, no periodicity is present along this plane. That staten, please note that, when in the following we will refer to the homogeneous data also the case of propagation in the patterned sample with wave vector parallel to grooves will be implied.

4.2 Propagation perpendicular to the grooves

A completely different scenario is that related to the measurements with wave vector perpendicular to grooves. Fast Fourier transforming the temporal signal measured at different induced wave vectors, we characterize the relation dispersion of the PC. Some general comments over the raw data are worth.

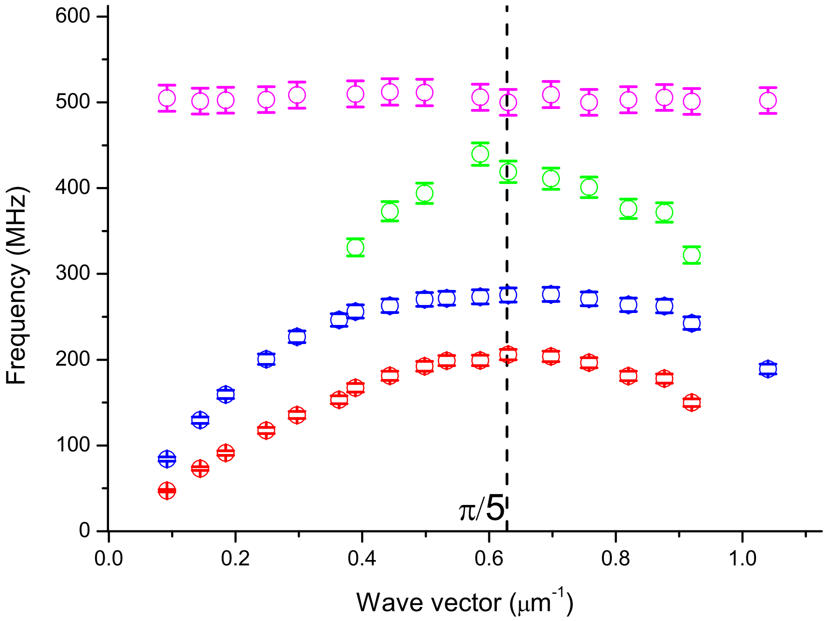

Figure 4.8: Measured dispersion on the grooved region, when the wave vector is induced perpendicularly to the grooving. Red and blue circles (we will generally refer to these as first and second mode respectively) are analogue to those modes observed in the homogeneous region. Green circles and magenta circles are respectively third mode and fourth mode and do not have any counterpart in the homogeneous region. Vertical dashed line is in correspondence of the band edge wave vector.

On the whole up to four modes are detected as shown in Fig. 4.8. First and second order mode resemble that of the homogeneous sample while the third, whose extent has a limited wave vector range, and the fourth, substantially flat, do not have any counterparts in the homogeneous case.

Even at a first look, Fig. 4.8 clearly shows the crystal-like nature that mechanical waves experience while propagating in the periodically corrugated surface: the symmetry of the dispersion curves with respect to the Brillouin zone boundary (the band edge at $q_B = \pi/5\ \mu\mathrm{m}^{-1}$) is its evidence. This behaviour is truly the sign of the crystal-like nature of the investigated sample. The TG experimental technique is able to realize such an accurate characterization of the dispersion relation, that in this frequency range would have been a hard task with Brillouin light scattering experiments due to central elastic peak (Rayleigh peak, that, on the other hand, do not give insight on Rayleigh waves..). Other experiments such as picosecond-ultrasonic couldn't put in evidence this peculiarity of the PC system as that technique does not allow, in contrast with TG, to have control over the induced wave vector. This crystalline behaviour, that is well known for real crystal (atomic order), was proven for PC in the micrometric range only in year 2000 [29]. Since then, as already discussed in the first chapter just one experimental paper has followed [30]. For the first time, in this Ph.D thesis, wave vectors of magnitude even 1.7 times bigger than the band-edge have been induced over a PC, experimentally confirming that the crystal like nature still holds for waves characterized by a wave vector roughly two times bigger than the band edge value.

It is interesting to have a look at the signals (Fig. 4.9), and their relative FFT power spectra (Fig. 4.10), related to two symmetric (with respect to the band edge value obviously) wave vectors $q = 0.50\mu m^{-1}$ (*below* the band edge) and $q = 0.76\mu m^{-1}$ (*above* the band edge). We observe that the signals' temporal evolution are far from being similar, and this could be somehow surprising as we have just underlined that the experimentally measured frequencies of symmetric wave

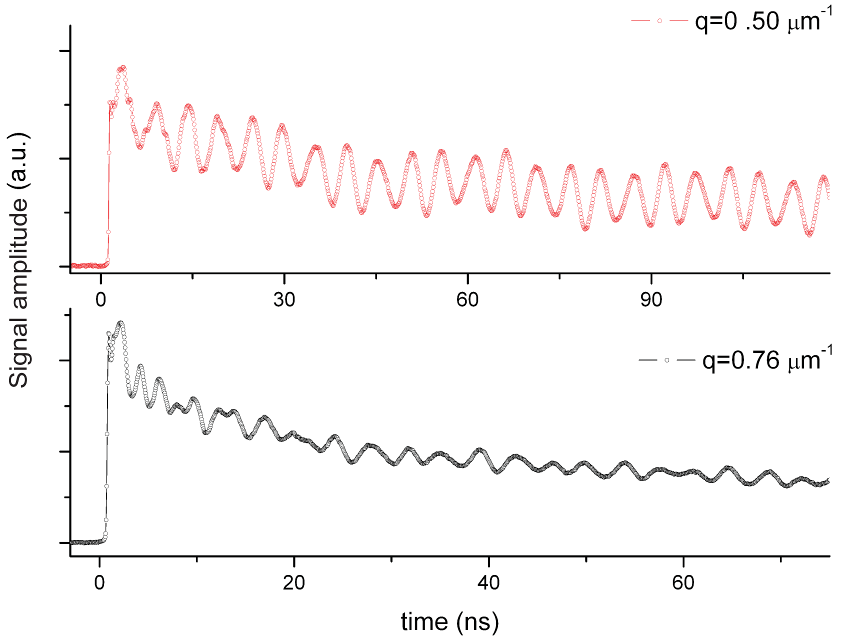

Figure 4.9: The temporal evolution of the signals relative to $q = 0.50\mu m^{-1}$ (in red, upper graph) and $q = 0.76\mu m^{-1}$ (in black, lower graph)

.

vectors yields the same values; thing which is confirmed by the spectra presented in Fig. 4.10 where we can see that, tough with a different structure, the frequency content for two wave vectors is the same. The different temporal evolution is explained in terms of that difference. In fact even though the measured frequencies are unvaried between the two cases, this do not hold for the amplitudes of peaks so that the different time evolution results from the different amplitude contribution of each excited mode. Practically we notice that the peak amplitude of the first order mode diminishes as much as the induced wave vector exceeds the band edge wave vector at gain of second and third order modes.

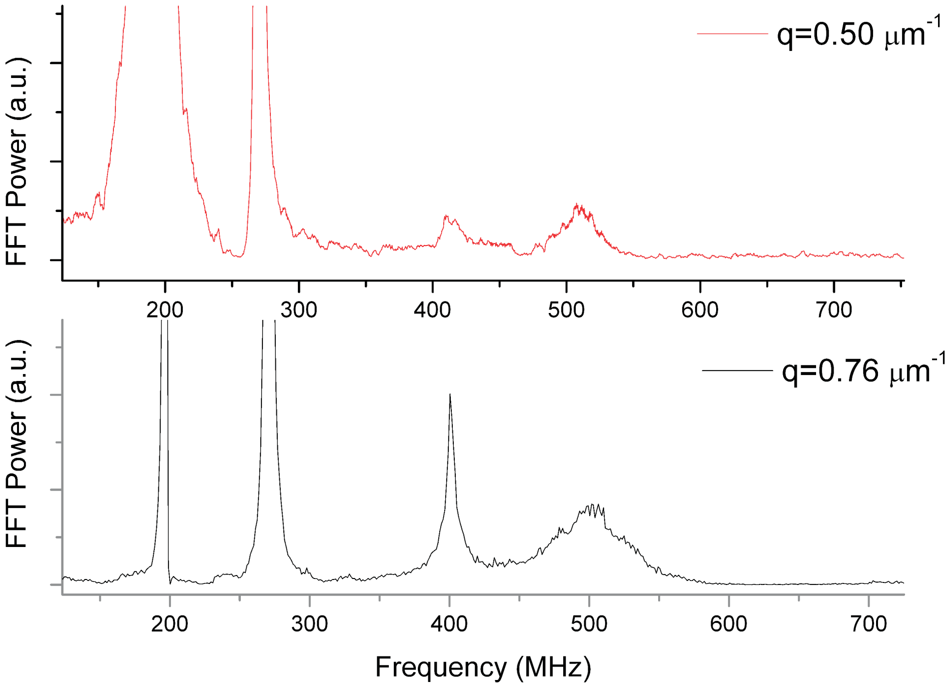

Figure 4.10: The FFT power spectrum of the signals reveals that the frequency content is, within the errors, the same

.

Given the crystalline behaviour, it is helpful to plot the dispersion curves versus the reduced wave number as in Fig. 4.11. The measured dispersion is consistent with the simulations, continuous lines in Fig. 4.11, that we realized over the Wigner-Seitz cell. In particular we want to stress that simulations of eigenmodes allow for direct visualization of the associated displacement field, which will result helpful in order to address the specific peculiarity of each mode. Both the data and simulations show a separation of about 70 MHz at the band edge between the first and second mode, anyhow this is not a band gap in the density of states, as the second order mode bends down in frequency and overlap with this. Two real

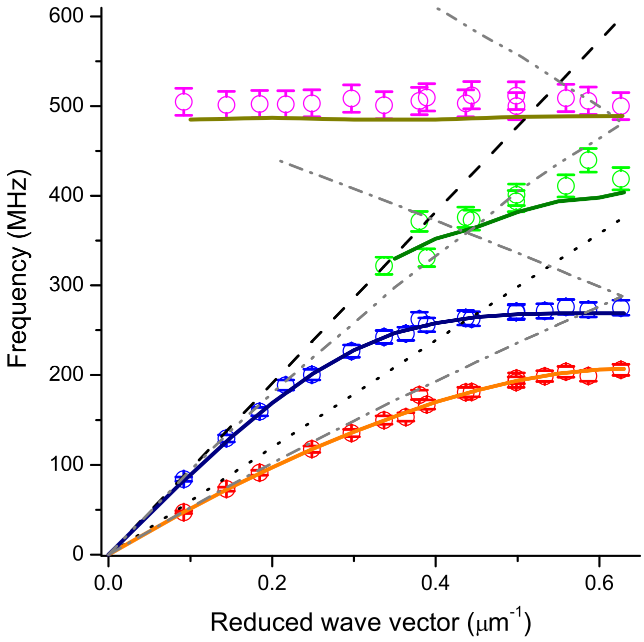

Figure 4.11: The data have been reduced to the first Brillouin zone. Continuous coloured lines represent the simulated dispersion curves for the PC, folded dispersion curves of the homogeneous sample (Rayleigh and Sezawa mode) are re-plotted as lines (dot-dash and dot-dot-dash respectively), black dotted (dashed) line correspond to the bulk transverse (longitudinal) mode in the substrate.

band gap are observed: one between the second and the third mode of approximately 55 MHz and the other between the third and the fourth mode of about 80 MHz. Some more words about the band gaps are needed, in fact we would have expected a much larger band gap inside the Brillouin zone. This, as observed by Maznev in [30], should have originated as a result of the “avoided crossing” between the homogeneous region Sezawa and zone folded Rayleigh modes (re-plotted in Fig. 4.11 as dash-dot-dot and dash-dot lines respectively). Its frequency gap would have been of about 220 MHz. A more detailed analysis of some analogue

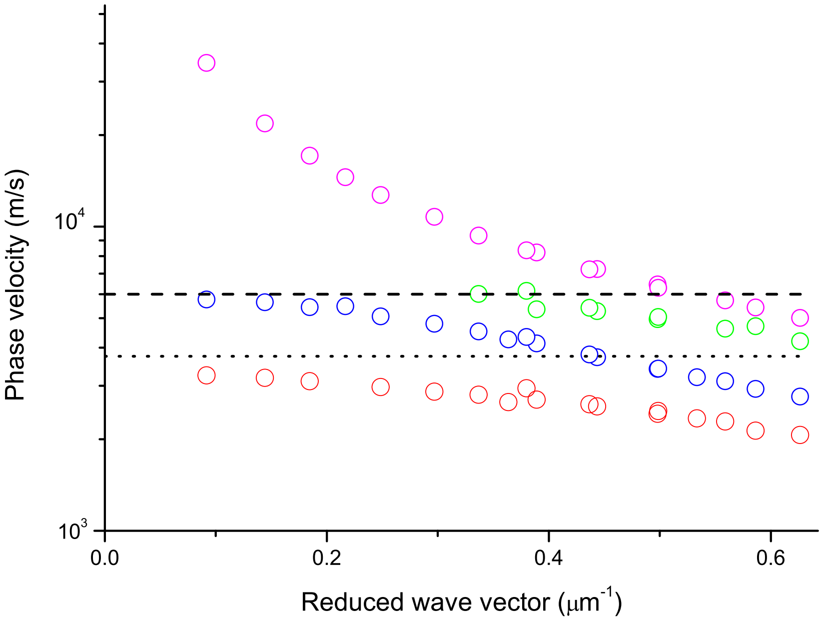

Figure 4.12: Phase velocities versus wave vector in the reduced zone scheme. Red, blue, green and magenta circles correspond to first, second, third and fourth mode respectively. Only the fourth mode phase velocity extends beyond the longitudinal bulk velocity of the substrate. Dotted (dashed) line corresponds to transverse (longitudinal) bulk phase velocity of the substrate.

samples where only pure SAW are excited (say the same sample with a thicker film) would help to have a deeper comprehension of this phenomenon.

In Fig. 4.12 we plot the phase velocities deduced from dispersion relation in the reduced zone scheme. We observe that the second order mode (blue circles) cross the SAW cutoff (dotted horizontal line) at a value $q \sim 0.44 \mu m^{-1}$.
The third order mode starts to be detected at a reduced wave vector value of $q \sim 0.33 \mu m^{-1}$ with a velocity which is that of the longitudinal bulk velocity (dashed horizontal line), as much as the second order mode does at lower q values.

We wonder if this third order mode is somehow to be attributed to a frequency lowering (induced by the surface structuring) of the third order mode present in the homogeneous simulation shown in Fig. 4.7. In fact, two interpretation of the nature (apart its undoubted PSAW character) of this mode are possible: whether it is an *optical* mode (where the word optical is used in analogy with the optical mode of a diatomic chain) or it is an *acoustic* mode (meaning that its frequency tends to zero as the wave vector tends to zero). The fact that we detect it exactly in correspondence of the longitudinal bulk values let us be in favour of the latter hypothesis, since, if it would be an optical mode, no restriction would apply to its phase velocity.

Finally the fourth mode shows an impressive phase velocity well above that of the longitudinal bulk velocity and its nature is evidently not acoustic.

Comparing the dispersion relation of the homogeneous sample with the first two observed modes (Fig. 4.11) it is evident the importance that metamaterial could cover in order to manipulate the mechanical parameters. In fact from the constituent materials point of view, nothing is changed with respect to the homogeneous case. It is just the realization geometry that alters so much the effective mechanical parameters, so that, for example, the second order mode, that had a PSAW character in the homogeneous sample throughout all the investigated wave vector range, becomes a SAW, in the PC, already at $q = 0.44 \mu m^{-1}$ and its frequency at the band edge is roughly half of that of the homogeneous sample at the same wave vector ($q_{BE} = 0.628 \mu m^{-1}$). Engineering the design would result in extracting the desired properties from bulk materials.

4.2.1 Rayleigh and Sezawa mode analysis

Lets now turn the attention on the first (Rayleigh) and second order (Sezawa) mode. These are the analogue of those observed in the homogeneous region. The

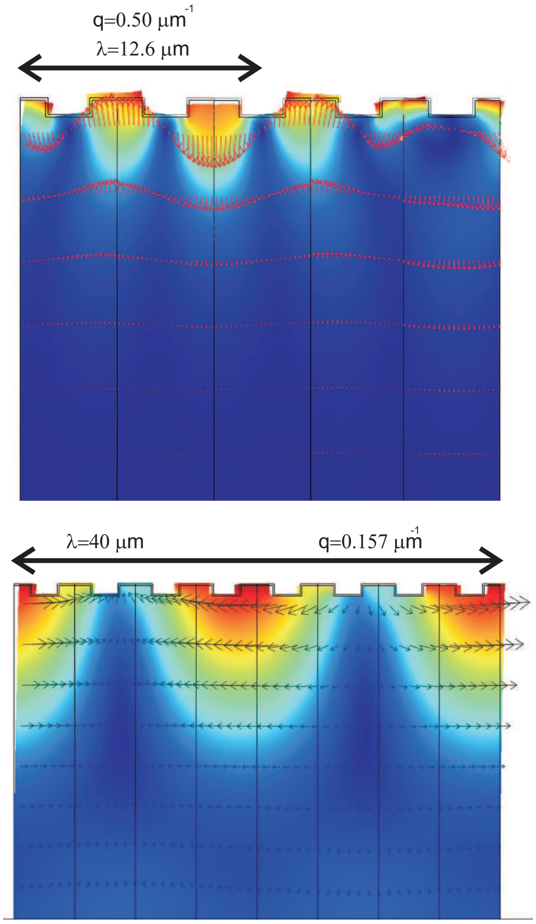

Figure 4.13: Displacement field associated to the second order at different wave vector. Bottom: displacement field characteristic of PSAW for $q = 0.157\mu m^{-1}$. Top: SAW characteristic displacement field for$q = 0.5\mu m^{-1}$.

effect of the surface structuring is to lower the frequency of both modes. The two modes flatten as the wave vector tends to the band edge, so that their group velocity reaches a null value leading to non propagative modes, we will consider this in section 4.2.3.

As already said the second mode changes its superficial character along the wave vector span at $q = 0.44\mu m^{-1}$. It is a PSAW for wave vectors under this value and become a SAW for wave vectors above this value. It can be instructive to plot its displacement field for the two cases (Fig. 4.13). Bottom part shows a mainly longitudinal displacement field, and a not at rest condition in depth of the material, that is typical of PSAW. By the way there are many similarities to that commented in the homogeneous sample section 4.1. This is not surprising in fact the wavelength is eight times the lattice step, then much bigger than both the depth of the grooving and the lattice step itself. Top part of Fig. 4.13 shows on the contrary a typical SAW displacement field: it is mainly transverse as testified by the arrows, and no motion in the depth is present. A supplementary comment over this displacement field may be worth. In fact it may be surprising that the displacement field does not repeat periodically with the wavelength. It is not, in fact, at $q = 0.5\mu m^{-1}$ the wavelength is not a multiple of the lattice step, it then follows that considering two points at the same depth and at a distance λ they won't be in the same relative position with respect to the cell. Then the displacement associated to the two points will be differently affected by the structure, so that the displacement doesn't have the wavelength periodicity. This can be easily understood in terms of the following arguments: the simulation realizes the displacement field $\mathbf{u_q}(\mathbf{r})$. So that the solution at a point $\mathbf{r}+\mathbf{R}$, where $\mathbf{R}$ is a generic direct lattice vector will differ by a phase according to Bloch theorem

$$\mathbf{u_q}(\mathbf{r}+\mathbf{R}) = \mathbf{u_q}(\mathbf{r})e^{-i(\mathbf{q}\cdot\mathbf{R})} \tag{4.1}$$

To clarify the above statements we plot in bottom part of Fig. 4.14 the horizontal (black) and vertical (red) displacement (at a fixed depth in the very proximity of the surface) as a a function of the x axis for the wave vector $q_1 = 0.157\mu m^{-1}$, and in bottom of Fig. 4.15 the same quantities for the wave vector $q_2 = 0.5\mu m^{-1}$. From Fig. 4.14 we immediately see that for the lower wave vector the horizontal displacement is predominating over the vertical displacement consistently with its PSAW character, while the inverse hold in Fig. 4.15 for q_2 (consistently with its SAW character). Moreover the horizontal displacement for the wave vector

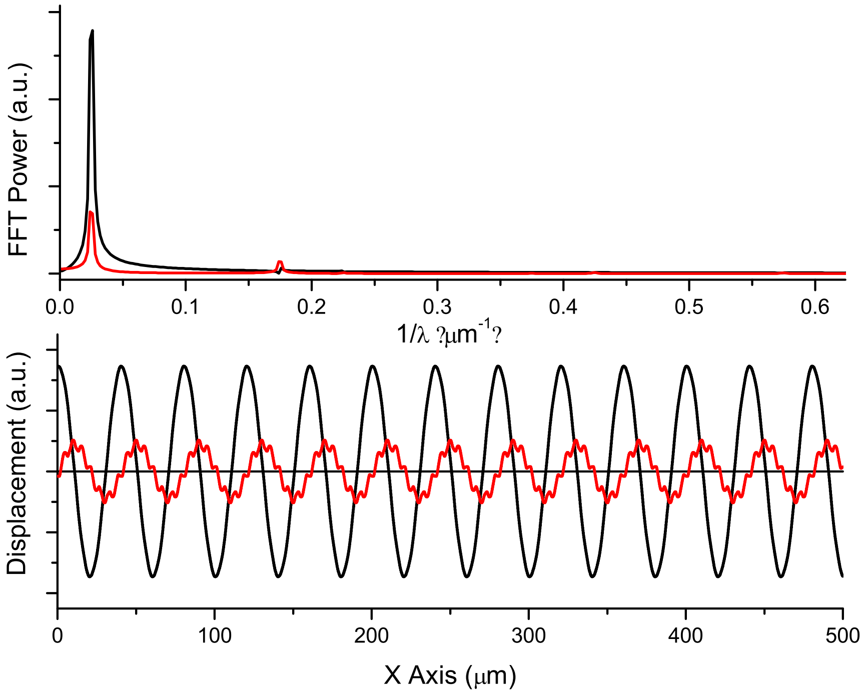

Figure 4.14: Bottom: Displacement components at $q_1 = 0.157\mu m^{-1}$ as a function of X direction. In black (red) horizontal (vertical) displacement. The periodicity is well defined by the associated wavelength and correspond to eight times the lattice step ($40\mu m$). Top: Corresponding Spatial FFT. Both horizontal and vertical displacement have a principal peak at $2\pi/q_1$, the peak at higher spatial frequency corresponds to the symmetric wave vector $q_1\prime$(see text).

q_1 (corresponding to a wavelength $\lambda = 40\mu m$) is substantially a pure sinusoidal function (with period λ) as it can be seen from its associated spatial FFT power shown in top part of Fig. 4.14,confirming that the surface structuring substantially doesn't affect the horizontal displacement at such long wavelength. Also the vertical displacement has a well defined period but, on the other hand, shows a second contribution in the spectra since it is the vertical displacement that is more affected from the surface structuring. This second peak (even though much less intense then the principal one) arises from the wave vector symmetric, with respect to the band edge, to q_1 which is $q_1\prime = 2q_{BE} - q_1$. This is consistent with the previously discussed reduced zone scheme. Other information can be obtained from the plots of Fig. 4.15. Concentrating on the bottom part of it we see that the displacements (both horizontal and vertical) do not show a sinusoidal profile. We already attribute that to the fact that the wavelength considered here ($\lambda \sim 12.6\mu m$) is not a multiple of the lattice step so that this mismatch prevents the displacement

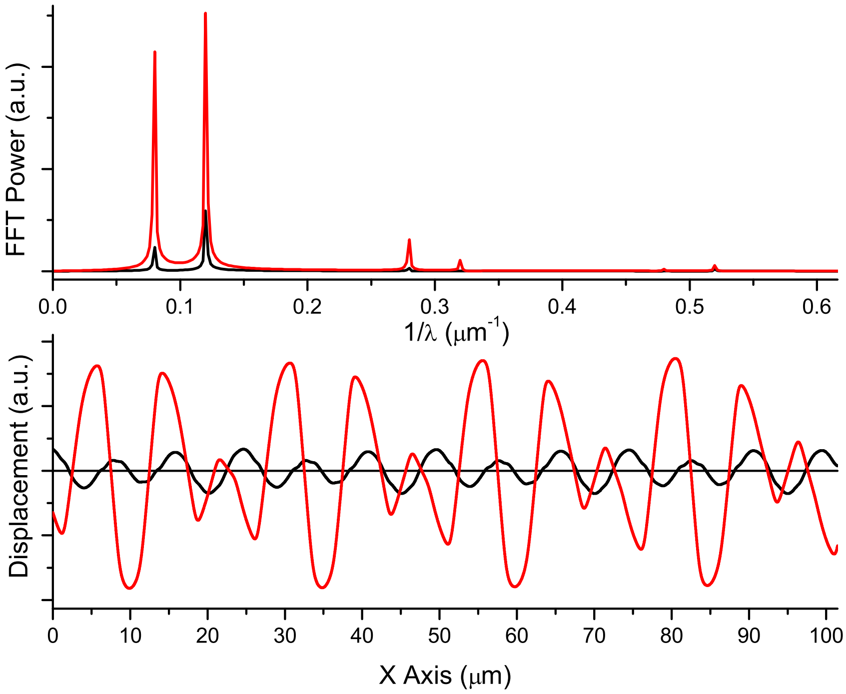

Figure 4.15: Bottom: Displacement components at $q = 0.5\mu m^{-1}$ as a function of X direction. In black (red) horizontal (vertical) displacement. Top: Corresponding Spatial FFT. Both horizontal and vertical displacement shows several peaks (see text).

field from having the wavelength periodicity. Another interesting feature is seen in top part of Fig. 4.15. In fact here, not only the two contribution from q_2 and its symmetric wave vector $q_2\prime = 2q_{BE} - q_2$ are observed, but also other are peaks are present. Where do they arise from? This peaks are the contributions of the Bloch harmonics relative to q_2 and $q_2\prime$. In fact, the displacement, say the vertical displacement u_y (but the same holds for the horizontal), of a mode propagating along the x axis with wave vector q can be represented, dropping the temporal term, by a superposition of Bloch harmonics [30]

$$u_y = \sum_{n=-\infty}^{n=+\infty} A_n e^{i[(q+\frac{2\pi n}{a})x)} \tag{4.2}$$

whose peaks are those observed in top part of Fig. 4.15.

4.2.2 Structures of modes at the band edge

The plots shown in Fig. 4.16 are instructive, for we can appreciate the different character of each of the detected modes. From this plots we extrapolated cross-sectional displacement field, along both the horizontal (Fig. 4.16), and the vertical direction (Fig. 4.17). We clearly distinguish the SAW character of the first and second order mode. The third mode character is more ambiguous. In fact it is by definition a PSAW (its phase velocity is above the threshold, see Fig. 4.12) still both its decay profile and the ratio between the amplitude of the longitudinal and horizontal oscillation do not fully confirm this thesis. In fact even tough the non zero value around which it oscillates in deep bulk is that typical of PSAW, the initial decay is not so “fast” as that typical of leaky waves, as shown for the homogeneous sample, but resemble that of first and second order mode, two pure SAW. Finally the ratio between the maximum horizontal and vertical displacement is that characteristic of SAW, as a matter of fact the polarization is mainly transverse.

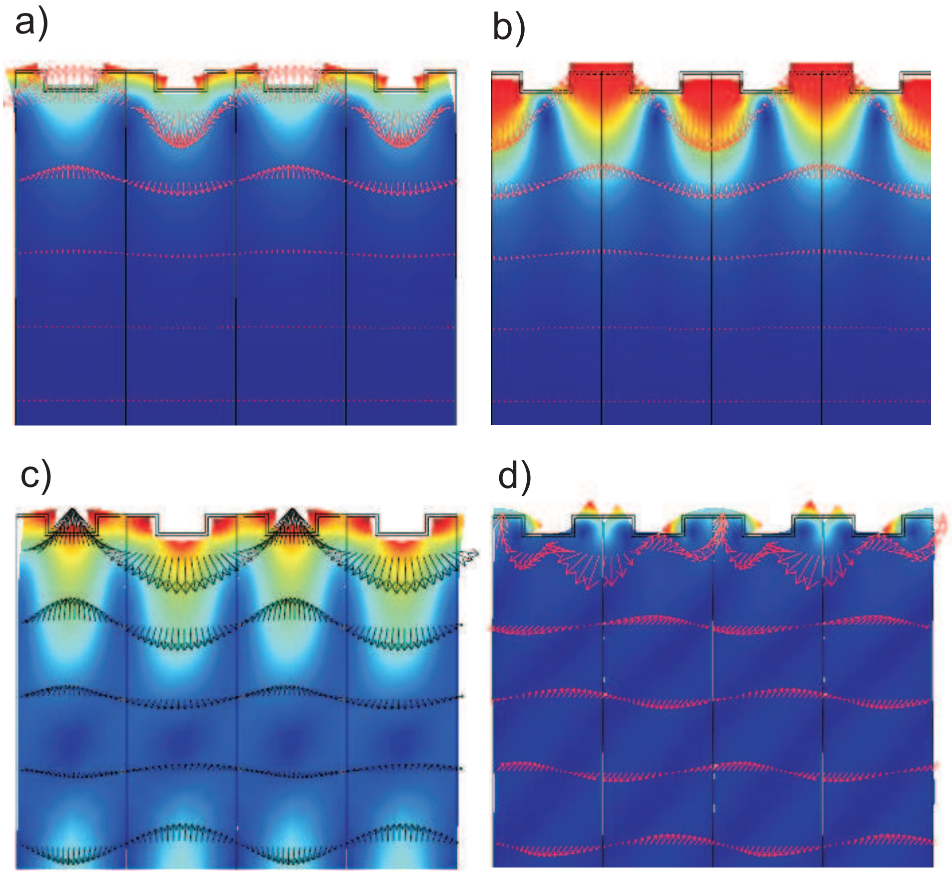

Figure 4.16: a) Band edge vectorial displacement field (plotted by arrows), and total displacement field (in colour scale), relative to first mode. Plot b), c) and d) are those of second, third and fourth order mode respectively.

The fourth mode is totally different from those just discussed. We notice that it is highly localized within the stair-steps that realize the superficial structure, so that the decay is much more rapid than that of both PSAW and SAW. Still its displacement involves also the substrate, as we can see from Fig. 4.17, since there is motion associated to this mode also in depth. This mode, to our opinion, is strictly correlated to the eigenmode of vibration of a single stair-step which we

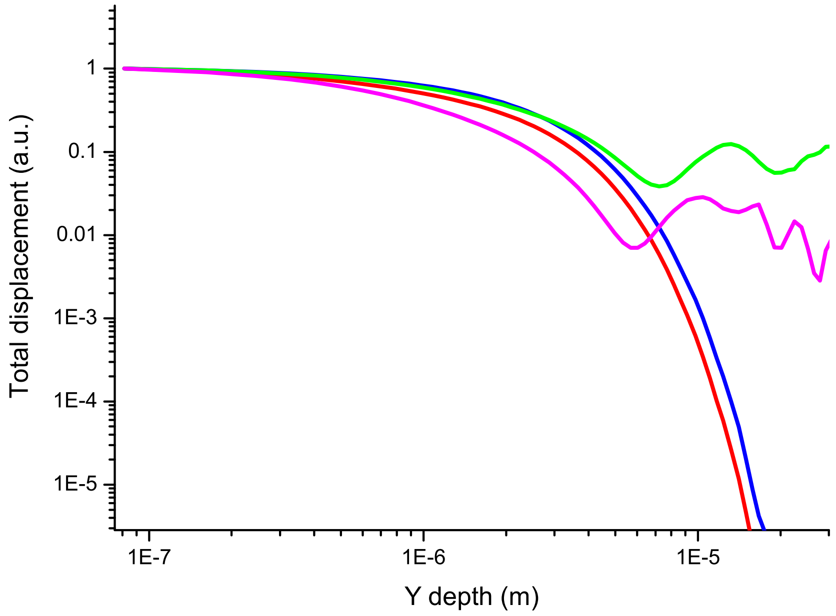

Figure 4.17: Total displacement as a function of depth in the material for the four modes present at the band edge. Red line and blue line (first and second order mode respectively) show a SAW typical decay profile, green line (third order mode) is the typical PSAW decayand magenta line to the fourth.

have simulated obtaining an eigenmode at about the same frequency. This single stair-step eigenmode then slightly varies its frequency (say a part over a hundred) and its displacement field when the simulation is realized over the entire sample resulting as an eigenmode of the whole structure. The plot of the displacement field along the horizontal direction (black line for the horizontal displacement, red line for the vertical displacement and green line for the total displacement), obtained as an horizontal cross section at a depth corresponding to the lower part of the surface (Fig 4.16), shows that the first mode has the maxima of the total displacement on the corners of the stair-steps and the minima in their center, (in

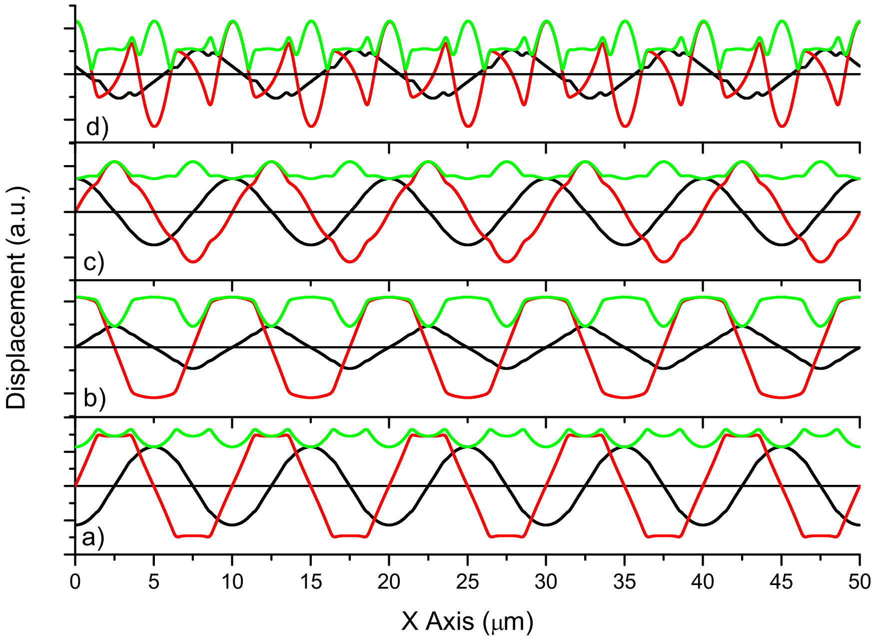

Figure 4.18: Horizontal (vertical, total) displacement, at a fixed depth in the material, as a function of the horizontal axis is plotted with black (red, green) continuous line for each of the mode detected (a=1st mode, b=2nd mode, etc.)

fact the vertical displacement posses nodes in the central part of the stair-steps). Conversely the second order mode has total displacement maxima in correspondence of the center of the stair-steps and the minima in the cental lower part of the superficial structure (the vertical displacement in this case posses nodes in the center of the chosen WSC). The third mode is similar to the first in fact has its minima at the center of the stair-steps but realizes the maximum total displacement in correspondence of the central lower part (where the second mode had the minima) instead that in the corner of the stair-steps.

4.2.3 Group velocity

As it is well known the *group velocity* $\mathbf{v}_g$ associated to a dispersive mode is defined, for a generic wave vector $\mathbf{k} = (k_x, k_y)$, as

$$\mathbf{v}_g = (\frac{\partial\omega}{\partial k_x}, \frac{\partial\omega}{\partial k_y}) \tag{4.3}$$

In a TG experiment the induced wave vector can be considered as one dimensional, say $\mathbf{k} = (k_x, 0)$, then $v_g = \partial\omega/\partial k_x$.

That staten it is immediately understood that the group velocity associated to a generic mode can be obtained as the derivative of the measured dispersion curve. However this is not a direct measurement of the group velocity. In order to realize an accurate direct measurement of the group velocity associated to the acoustic wavepacket it is convenient to displace the probe spot from the pump spot along the direction where the grating is realized, so that the ratio between the relative displacement of the two spots S and the measured arrival time t of the acoustic wave packet is a direct measurement of the group velocity $v_g = S/t$. We have then slightly modified our setup. The cylindrical lens that focused the pump spot has been removed and replaced by a simple convergent lens. To allow the relative displacement of the two spots the mirror M in front of the exit of the probe laser, has been mounted over a translating stage in order to realize the displacement (along the direction where the grating is realized) between the two spots .

We have realized the measurements for different values of the experimental wave vector ($q = 0.50\mu m^{-1}$, $q = 0.55\mu m^{-1}$ and $q = 0.63\mu m^{-1} \simeq q_{BE}$) both in the homogeneous sample and the PC. In Fig. 4.19 we show the signals obtained on the homogeneous sample for different relative displacements of the two spots (in black the measurement when the spots are overlapped) at the wave vector $q = 0.50\mu m^{-1}$: the arrival time of the wavepacket, that we define to be that corresponding to the maxima of the wavepacket, increases as the distance between the two spots is augmented as illustrated in Fig. 4.21. The same behaviour is also present in the homogeneous sample investigated at $q = 0.63 \mu m^{-1}$.

The typical wavepacket is shown in the inset of Fig. 4.19 together with the fit that we performed in order to determine the arrival time. The fit function that we employed is given by the product of a gaussian distribution (the envelope of the wavepacket) determined by the laser spot, and a sinusoidal function (oscillating at the frequency of the propagative mode). The same behaviour is also present when the homogeneous sample has been investigated at $q = 0.55 \mu m^{-1}$ and $q = 0.63 \mu m^{-1}$.

Then the PC was taken in analysis. At the wave vectors $q = 0.50 \mu m^{-1}$ and $q = 0.55 \mu m^{-1}$ the trend is qualitatively the same observed in the homogeneous sample: the signal is observed both when the probe and pump spots are overlapped and when are displaced, as shown, for $q = 0.50 \mu m^{-1}$, in the upper part of Fig.4.20.

A totally different scenario is that related to the wave vector $q = 0.63 \mu m^{-1} \simeq q_{BE}$. For this wave vector value, the signal is only obtained when the two spots are overlapped, while no signal is detected when the analysis is realized over the travelling wavepacket (the two spots aren't overlapped). This is consistent with a nearly zero group velocity of the wavepacket. In fact the modes at the band edge are characterized by a null group velocity and do not propagate, so that, when the probe is displaced from the pump, there is no any travelling wavepacket that reaches the probe spot to produce the signal.

The displacement S is linearly dependent on the arrival time t, the slope of the linear fit is a direct measurement of the group velocity. In Fig. 4.21 the results obtained both for the homogeneous sample and the PC at $q = 0.50 \mu m^{-1}$, $q = 0.55 \mu m^{-1}$ and $q = 0.63 \mu m^{-1}$ are presented.

The measured group velocities are in good agreement with those obtained from

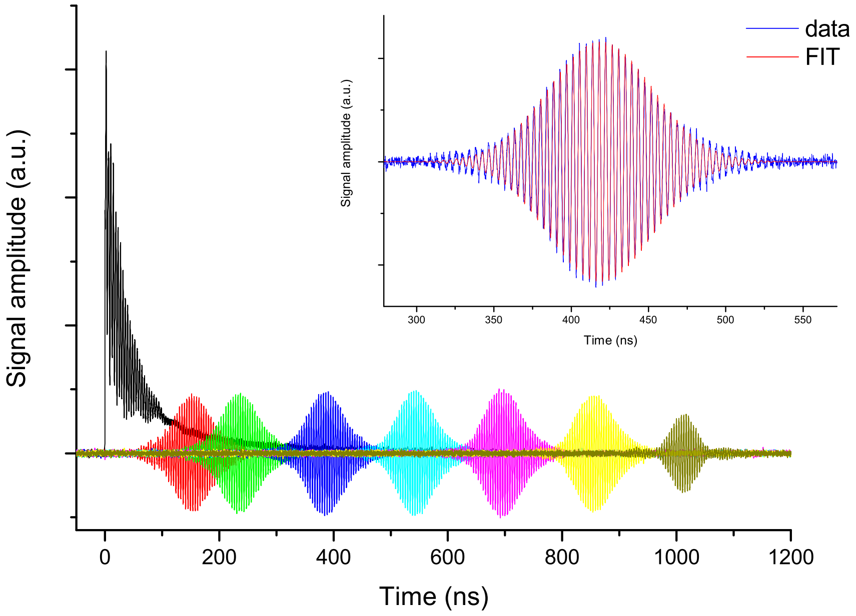

Figure 4.19: Measured signals in the homogeneous region at $q = 0.50\mu m^{-1}$ for different relative displacements of the probe and the pump spot. In the inset the typical signal associated to the travelling wavepacket is shown. The envelope of the signal is the gaussian spot of the laser, while the fast oscillations have the frequency of the associated mode(s).

the differentiation of the dispersion curve of the first amd second order modes of both the homogeneous and the PC sample (see Fig. 4.22). As it can be observed the measured values are those relative to the first mode only, since the excited travelling wavepacket spectra contribution are dominated by the first order mode.

Using this experimental technique we clearly show a strong reduction of the group velocity that is approaching zero when q coincide with q_{BE}. In order to attempt a direct measure of $v_g(q_{BE})$ we can follow a different approach.
As already mentioned in section 2.2 the group velocity is that responsible of the

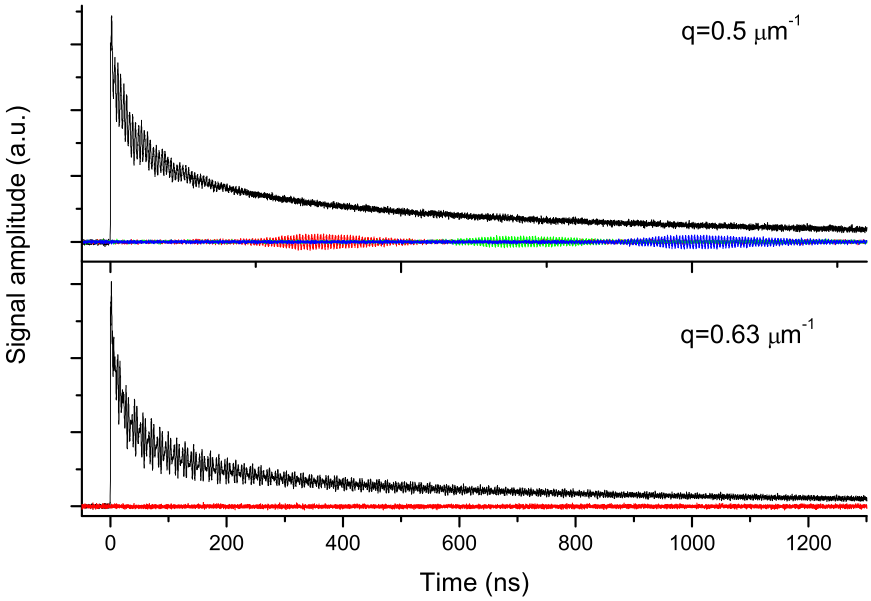

Figure 4.20: Measured signals in the PC for different relative displacements of the probe and the pump spot for the two wave vectors. While in the case of $q = 0.50\mu m^{-1}$ (upper part) the behaviour is analogue to that of the homogeneous region, at the value $q = 0.63\mu m^{-1} \simeq q_{BE}$ (lower part) no travelling wavepackets are observed at any time. This is consistent with a zero group velocity.

oscillations decay in the transient grating experiment when the decay is dominated by the walk-off of the acoustic wavepackets. The associated walk-off time is $\tau = d/v_g$, where $2d$ is the excitation spot size. This offers an alternative method to measure the group velocity in those measurements realized with the pump and probe spots overlapped, once that the walk-off time and the pump spot width are determined.

The dimension of the pump spot $2d$ has been obtained by means of the travelling wavepacket shown in the inset of Fig. 4.19. The pump spot width is defined as the product of the temporal width of the travelling wavepacket and its group velocity

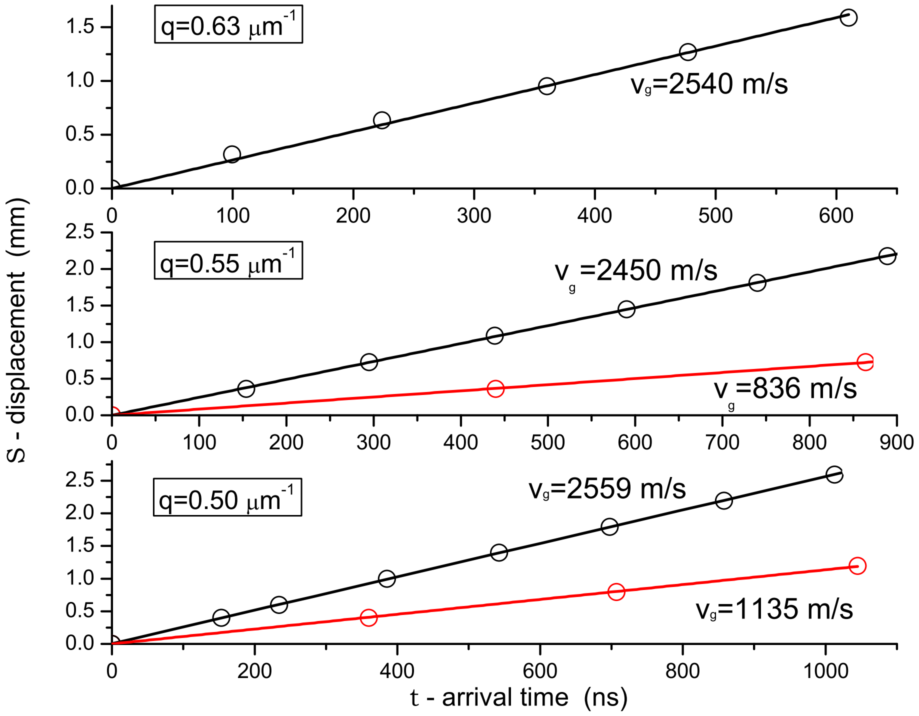

Figure 4.21: Displacement between the pump and probe spot S as a function of the arrival time t for $q = 0.50\mu m^{-1}$ (lower part), $q = 0.50\mu m^{-1}$ (middle) and $q = 0.63\mu m^{-1}$ (upper part). Black (red) circles are the experimental data for the homogeneous sample (PC), continuos line are the relative linear fit.

(just measured). The temporal width of the wave packet was obtained by means of the FFT tool, as explained in what follows. Finally the spatial width of the spot results $2d \sim 500\mu m$.

We can measure the walk-off time from the measured signal, simply determining the time at which no oscillations are seen in the signal. This can also be done more elegantly by means of the FFT, as it has also been done, to estimate the temporal extension of the oscillations of the travelling wave packet in order to obtain the pump spatial width. The temporal extension of a signal (be it that of the travel-

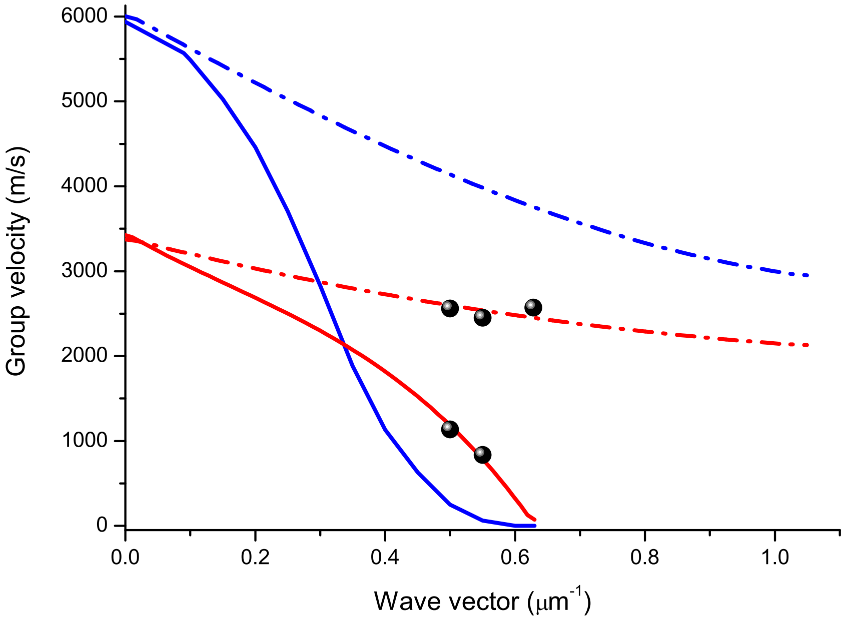

Figure 4.22: Black full circles are the experimentally measured group velocities. Continuous (PC) and dash-dotted (homogeneous sample) lines are the simulated group velocities obtained as the derivative of the simulated dispersion curves multiplied by a factor 2π. Red refers to first order modes and blue to second order modes.

ling wavepacket, or that obtained with the pump and probe spots overlapped) is obtained by the following procedure: subdivide the whole measured signal temporal evolution (e.g. $1\mu s$) in time intervals of a properly chosen time window (e.g. $100ns$); perform the FFT within each interval until an interval, whose FFT peak's magnitude is about 2% that of the peak obtained in the first interval, is found (e.g. time interval $700-800ns$). The walk-off time can be defined as that corresponding to half of the latter interval ($750ns$).

In Fig. 4.23 the measurement at $q \simeq q_{BE}$ realized in the homogeneous sample

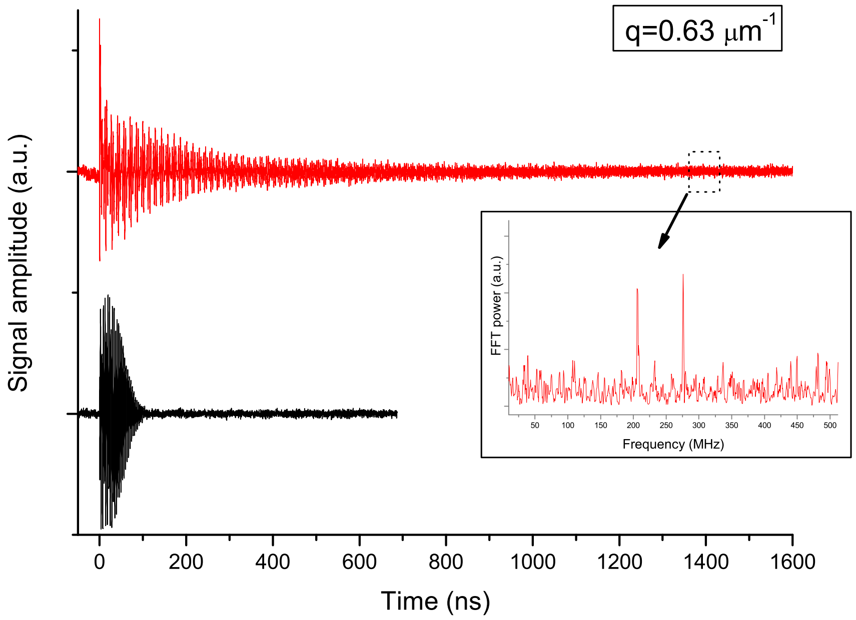

Figure 4.23: Signal temporal evolution obtained at $q \simeq q_{BE}$ for the homogeneous sample (black) and the PC sample (red). The temporal scale over which the signal associated to the PC sample evolves, is more than a order of magnitude than that of the homogeneous. In the inset the FFT power associated to the walk-off measured time.

(black) and the PC (red) are shown. The thermal contribution to both signals has been subtracted by means of a fit in order to clearly show and appreciate the oscillating contribution. It is impressive the different timescale over which the walk-off realizes in the two cases. This is due to the large difference between the group velocity of the samples, in fact the excited wave vector is nearly the band edge wave vector, that nominally implies a null group velocity for the PC. With the estimated walk-off times we obtain a value of $v_g = 2490 m/s$ for the homogeneous sample and a extraordinary slower value for the PC $v_g = 180 m/s$. This latter value is evidently not zero, however this can be justified in terms of the uncertainty over

the excited wave vector. In fact, a slight uncertainty of a $\sim 1\%$ over the nominal value of q_{BE}, that we admit to have, would justify the measured group velocity.
We note that an attempt to measure slow waves by means of the walk-off time has been realized within a recent paper [48]. However no evidence of these slow waves was reported. In the paper the fact is attributed to an inhomogeneous broadening arising from various factors such as scattering due to surface roughness, polycristalline structure of the metal film, and the deviation of the structure from the exact periodicity, both in the lattice step, the width and the eight of the stair-steps.

4.3 Concluding Remark

In this work we have characterized the propagation of surface acoustic waves in a fused silica plate composed of two distinct regions: an homogeneous region and a grooved one. The experimental characterization of the dispersion relation of the homogeneous sample and that of the grooved sample, in the two opposite case of wave vector parallel or orthogonal to the grooving, has been realized with a transient grating experiment.
The characterization has been realized not only experimentally, but also theoretically. The theoretical analysis has been performed with a commercial software, that showed to be a good and reliable tool to perform band diagram characterization. The insight given by the simulations on the surface waves allowed to unambiguously characterize the observed modes, both in their frequency and their spatial form (the displacement field).
We have observed that the waves propagating in the homogeneous sample are composed of two modes. The same holds for the waves propagating in the grooved region with wave vector parallel to the grooves. The experimental data were in

good agreement with the simulations.

When the waves are induced in the grooved sample with wave vector orthogonal to the grooved region, the dispersion relation greatly alters from the preceding case. Waves are affected by the periodically patterned surface and their dispersion relation becomes that typical of crystals: band diagram. In fact a band edge wave vector was experimentally identified and the number of observed modes was increased. Also in this case the agreement between the simulations and the experiment was really satisfying.

Finally direct measurements of the group velocity have been performed. In these the very first observation of really slow waves has been obtained around the band edge wave vector.

Bibliography

[1] E.Yablonovitch. *Phys. Rev. Lett.* **58**, 2059 (1987).

[2] S.John. *Phys. Rev. Lett.* **58**, 2486 (1987).

[3] J.W.S.Rayleigh. *Phyl. Mag.* **26**, 256 (1888).

[4] A.Khelif, A.Chouujaa, S.Benchabane, B.Djafari-Rouhani, and V.Laude. *Appl. Phys. Lett.* **84**, 4400 (2004).

[5] F.Cervera, L.Sanchis, J.V.Sánchez-Pérez, R.Martínez-Sala, C.Rubio, F.Meseguer, C.López, D.Caballero, and J.Sánchez-Dehesa. *Phys. Rev. Lett.* **88**, 023902 (2002).

[6] S.Zhang, L.Yin, and N.Fang. *Phys. Rev. Lett.* **102**, 194301 (2009).

[7] S.A.Cummer and D.Schurig. *New Jour. of Phys.* **9**, 45 (2007).

[8] M.Farhat, S.Guenneau, and S.Enoch. *Phys. Rev. Lett.* **103**, 024301 (2009).

[9] T.Gorishnyy, C.K.Ullal, G.Fytas, and E.L.Thomas. *Phys. Rev. Let.* **94**, 115501 (2005).

[10] B.Bonello, C.Charles, and F.Ganot. *Ultasonics* **44**, e1259 (2006).

[11] M.S.Kushwaha, P.Halevi, L.Dobrzysnki, and B.Djafari-Rouhani. *Phys. Rev. Lett.* **71**, 2022 (1993).

[12] M.S.Kushwaha, P.Halevi, G.Martínez, L.Dobrzynski, and B.Djafari-Rouhani. *Phys. Rev. B* **49**, 2313 (1994).

[13] E.N.Economu and M.M.Sigalas. *Phys. Rev. B* **48**, 13434 (1993).

[14] M.Kafesaki, M.M.Sigalas, and E.N.Economu. *Solid State Comm.* **96**, 285 (1995).

[15] R.Martínez-Sala, J.V.Sánchez, J., V.Gómez, J.Llinares, and Meseguer, F. *Nature* **318**, 241 (1995).

[16] J.R.Dutcher, S.Lee, B.Hillebrands, G.J.McLaughlin, B.G.Nickel, and G.I.Stegeman. *Phys. Rev. Lett.* **68**, 2464 (1992).

[17] S.Lee, L.Giovannini, J.R.Dutcher, F.Nizzoli, G.I.Stegeman, A.M.Marvin, Z.Wang, J.D.Ross, A.Amoddeo, and L.S.Caputi. *Phys. Rev. B* **49**, 2273 (1994).

[18] W.Cheng. *Nature Materials* **5**, 830 (2006).

[19] F.R.Montero, E.Jimenez, and M.Torres. *Phys. Rev. Lett.* **80**, 1208 (1998).

[20] D.Caballero, J.Sánchez-Dehesa, C.Rubio, R.Mártinez-Sala, J.V.Sánchez-Pérez, F.Meseguer, and J.Llinares. *Phys. Rev. E* **60**, R6316 (1999).

[21] J.O.Vasseur, P.A.Deymier, B.Chenni, B.Djafari-Rouhani, L.Dobrzynski, and D.Prevost. *Phys. Rev. Lett.* **86**, 3012 (2001).

[22] A.Sukhovich, L.Ling, and J.H.Page. *Phys. Rev. B* **77**, 014301 (2008).

[23] D.M.Profunnser, O.B.Wright, and O.Matsuda. *Phys. Rev. Lett.* **97**, 055502 (2006).

[24] H.T.Grahn, H.J.Maris, and J.Tauc. *IEEE J. of Quan. Ele.* **25**, 2562 (1989).

[25] H.N.Lin, H.J.Maris, K.Y.Lee, L., H.Luhn, and D.P.Kern. *J. Appl. Phys* **73**, 37 (1993).

[26] G.A.Antonelli. *J. Appl. Phys.* **91**, 3261 (2002).

[27] J.F.Robillard, A.Devos, I.Roch-Jeune, and P.A.Mante. *Phys. Rev. B* **78**, 064302 (2008).

[28] TailphoX european project, Available at http://www.tailphox.org.

[29] L.Dhar and J.A.Rogers. *Appl. Phys. Lett.* **77**, 1402 (2000).

[30] A.A.Maznev. *Phys. Rev. B* **78**, 155323 (2008).

[31] L.D.Landau and E.M.Lifshitz. *Course of Theoretical Physics*, volume Volume 7 - Theory of Elasticity. Pergamon Press, Oxford, New York, Toronto, Sydney, Paris, Braunschweig, (1959).

[32] J.A.Rogers, A.A.Maznev, M.J.Banet, and K.A.Nelson. *Annu. Rev. Mater. Sci.* **30**, 117 (2000).

[33] N.W.Ashcroft and N.D.Mermin. *Solid State Physics.* Saunders College, Philadelphia, (1976).

[34] N.Bloembergen. *Nonlinear optics.* Benjamin, New York, (1977).

[35] Y.R.Shen. *Principles of non-linear optics.* John Wiley & Sons, New York, (1984).

[36] AAVV. *Special issue on dynamic grating and four-wave mixing*, volume 22. IEEE J. Quant. Electron., (1986).

[37] H.J.Eichler, P.Gunter, and D.W.Pohl. *Laser-Induced Dynamic Gratings.* Springer-Verlag, Berlin, (1986).

[38] Y.Yan and K.A.Nelson. *J. Chem. Phys.* **87**, 6240 (1987).

[39] J.W.Goodman. *Introduction to Fourier Optics.* Mc Graw Hill, NewYork, (1996).

[40] A.Miklos and A.Lorincz. *J. Appl. Phys.* **63**, 2391 (1988).

[41] A.Taschin, R.Eramo, P.Bartolini, and R.Torre. *Time-resolved spectroscopy of complex liquids*, chapter Transient grating experiments in glass-former liquids, 129. Springer, New York (2008).

[42] A.A.Maznev, K.A.Nelson, and J.A.Rogers. *Opt. Lett.* **23**, 1319 (1998).

[43] G.D.Goodno, G.Dadusc, and R.J.D.Miller. *J. Opt. Soc. Am. B* **15**, 1791 (1998).

[44] M.Terazima. *J. Phys. Chem. A* **103**, 7401 (1999).

[45] S.Mukamel. *Principles of nonlinear optical spectroscopy.* Oxford University Press, New York, (1995).

[46] N.E.Glass and A.A.Maradudin. *J. Appl. Phys.* **54**, 796 (1983).

[47] D.Nardi, F.Banfi, C.Giannetti, B.Revaz, G.Ferrini, and F.Parmigiani. *Phys. Rev B* **80**, 104119 (2009).

[48] A.A.Maznev and O.B.Wright. *J. Appl. Phys.* **105**, 123530 (2009).